

## THE RADIO SKY AT METER WAVELENGTHS: *M*-MODE ANALYSIS IMAGING WITH THE OWENS VALLEY **RADIO OBSERVATORY** LONG WAVELENGTH ARRAY

MICHAEL W. EASTWOOD,<sup>1</sup> MARIN M. ANDERSON,<sup>1</sup> RYAN M. MONROE,<sup>2</sup> GREGG HALLINAN,<sup>1</sup> BENJAMIN R. BARSDELL,<sup>3, 4</sup>  
STEPHEN A. BOURKE,<sup>1, 5</sup> M. A. CLARK,<sup>4</sup> STEVEN W. ELLINGSON,<sup>6</sup> JAYCE DOWELL,<sup>7</sup> HUGH GARDEN,<sup>3</sup>  
LINCOLN J. GREENHILL,<sup>3</sup> JACOB M. HARTMAN,<sup>8</sup> JONATHON KOCZ,<sup>1</sup> T. JOSEPH W. LAZIO,<sup>9</sup> DANNY C. PRICE,<sup>3, 10, 11</sup>  
FRANK K. SCHINZEL,<sup>12, 7</sup> GREGORY B. TAYLOR,<sup>7</sup> HARISH K. VEDANTHAM,<sup>1</sup> YUANKUN WANG,<sup>1</sup> AND DAVID P. WOODY<sup>13</sup>

<sup>1</sup>Department of Astronomy, California Institute of Technology, 1200 E California Blvd, Pasadena, CA 91125, USA

<sup>2</sup>Department of Electrical Engineering, California Institute of Technology, 1200 E California Blvd, Pasadena, CA 91125, USA

<sup>3</sup>Harvard-Smithsonian Center for Astrophysics, 60 Garden Street, Cambridge, MA 02138, USA

<sup>4</sup>NVIDIA Corporation, 2701 San Tomas Expressway, Santa Clara, CA 95050, USA

<sup>5</sup>Department of Space, Earth and Environment, Chalmers University of Technology, Onsala Space Observatory, 43992 Onsala, Sweden

<sup>6</sup>Bradley Department of Electrical & Computer Engineering, Blacksburg, VA 24061, USA

<sup>7</sup>Department of Physics and Astronomy, University of New Mexico, Albuquerque, NM 87131, USA

<sup>8</sup>Google, 340 Main St, Venice, CA 90291, USA

<sup>9</sup>Jet Propulsion Laboratory, California Institute of Technology, 4800 Oak Grove Dr, Pasadena, CA 91109, USA

<sup>10</sup>University of California Berkeley, 501 Campbell Hall, Berkeley, CA 94720, USA

<sup>11</sup>Centre for Astrophysics & Supercomputing, Swinburne University of Technology, PO Box 218, Hawthorn, VIC 3122, Australia

<sup>12</sup>National Radio Astronomy Observatory, P.O. Box O, Socorro, NM 87801, USA

<sup>13</sup>California Institute of Technology, Owens Valley Radio Observatory, Big Pine, CA 93513, USA

### ABSTRACT

A host of new low-frequency radio telescopes seek to measure the 21-cm transition of neutral hydrogen from the early universe. These telescopes have the potential to directly probe star and galaxy formation at redshifts  $20 \gtrsim z \gtrsim 7$ , but are limited by the dynamic range they can achieve against foreground sources of low-frequency radio emission. Consequently, there is a growing demand for modern, high-fidelity maps of the sky at frequencies below 200 MHz for use in foreground modeling and removal. We describe a new widefield imaging technique for drift-scanning interferometers, Tikhonov-regularized *m*-mode analysis imaging. This technique constructs images of the entire sky in a single synthesis imaging step with exact treatment of widefield effects. We describe how the CLEAN algorithm can be adapted to deconvolve maps generated by *m*-mode analysis imaging. We demonstrate Tikhonov-regularized *m*-mode analysis imaging using the Owens Valley Radio Observatory Long Wavelength Array (OVRO-LWA) by generating 8 new maps of the sky north of  $\delta = -30^\circ$  with 15 arcmin angular resolution, at frequencies evenly spaced between 36.528 MHz and 73.152 MHz, and  $\sim 800$  mJy/beam thermal noise. These maps are a 10-fold improvement in angular resolution over existing full-sky maps at comparable frequencies, which have angular resolutions  $\geq 2^\circ$ . Each map is constructed exclusively from interferometric observations and does not represent the globally averaged sky brightness. Future improvements will incorporate total power radiometry, improved thermal noise, and improved angular resolution – due to the planned expansion of the OVRO-LWA to 2.6 km baselines. These maps serve as a first step on the path to the use of more sophisticated foreground filters in 21-cm cosmology incorporating the measured angular and frequency structure of all foreground contaminants.

*Keywords:* cosmology: observations – dark ages, reionization, first stars – radio continuum: galaxies  
– radio continuum: ISM

## 1. INTRODUCTION

At redshifts  $20 \gtrsim z \gtrsim 7$ , the 21-cm hyperfine structure line of neutral hydrogen is expected to produce a 10 to 100 mK perturbation in the Cosmic Microwave Background (CMB) spectrum (Furlanetto et al. 2006; Pritchard & Loeb 2012). The amplitude of this perturbation on a given line-of-sight is a function of the neutral fraction of hydrogen, the baryon overdensity, the spin temperature relative to the CMB temperature at the given redshift, and the line-of-sight peculiar velocity of the gas. The spatial power spectrum of this perturbation is thought to be dominated by inhomogeneous heating of the IGM at  $z \sim 20$  (Fialkov et al. 2014), and by growing ionized bubbles during the EoR at  $z \sim 7$  where a detection can constrain the ionizing efficiency of early galaxies, the UV photon mean-free-path, and the minimum halo mass that can support star formation (Greig & Mesinger 2015).

Current 21-cm cosmology experiments can be broadly separated into two classes: global signal experiments that aim to detect the spectral signature of the cosmologically redshifted 21-cm transition after averaging over the entire sky (otherwise known as the monopole), and power spectrum experiments that incorporate angular information to attempt to measure the 3D spatial power spectrum of cosmological 21-cm perturbations. Ongoing global signal experiments include EDGES (Monsalve et al. 2017), LEDA (Price et al. 2017), BIGHORNS (Sokolowski et al. 2015), SCI-HI (Voytek et al. 2014), and SARAS 2 (Singh et al. 2017). Ongoing power spectrum experiments include PAPER/HERA (Ali et al. 2015; DeBoer et al. 2016), LOFAR (Patil et al. 2017), and the MWA (Beardsley et al. 2016; Ewall-Wice et al. 2016). Recently, EDGES reported the first detection of 21-cm absorption in the globally averaged sky-signal (Bowman et al. 2018).

Just as for CMB experiments, foreground removal or suppression is an essential component of both classes of 21-cm cosmology experiments. The brightness temperature of the galactic synchrotron emission at high galactic latitudes is measured by Mozdzen et al. (2017) as

$$T \sim 300 \text{ K} \times \left( \frac{\nu}{150 \text{ MHz}} \right)^{-2.6}. \quad (1)$$

Therefore, experiments conservatively need to achieve 5 orders of dynamic range against this foreground emission before the cosmological signal can be measured. Current foreground removal methods (for example, Parsons et al. 2012 and Chapman et al. 2013) rely on the assumption that the foreground emission is spectrally smooth. The low-frequency radio sky is composed of several components: galactic synchrotron emission, su-

pernova remnants, radio galaxies, free-free emission and absorption from H II regions, and a confusing background of radio sources. Ideally, a foreground removal strategy should be informed by the measured spatial structure and frequency spectrum of all foreground components. For instance, CMB experiments typically construct several maps at several frequencies to enable component separation. At low frequencies, this possibility is limited by the availability of suitable high-fidelity sky maps on angular scales ranging from tens of degrees to arcminutes.

Recently, a host of new low-frequency sky surveys have been conducted including MSSS (Heald et al. 2015), GLEAM (Wayth et al. 2015), and TGSS (Intema et al. 2017). However, the primary data product generated by these surveys is a catalog of radio point sources. At 45 MHz, Guzmán et al. (2011) created a map of the sky that captures the diffuse emission with  $5^\circ$  resolution. The LWA1 Low Frequency Sky Survey (Dowell et al. 2017) similarly maps the sky at a range of frequencies between 35 MHz and 80 MHz with resolution between  $4.5^\circ$  and  $2^\circ$ .

The Global Sky Model (GSM) (de Oliveira-Costa et al. 2008) is currently the most commonly used foreground model. The GSM is a non-parametric interpolation of various maps between 10 MHz and 100 GHz. However, the majority of information contained in the GSM is derived at frequencies  $> 1.4$  GHz where the majority of the modern, high-fidelity input maps are located. At 408 MHz the venerable Haslam map (Haslam et al. 1981, 1982) covers the entire sky at  $1^\circ$  resolution. Below 408 MHz the GSM uses 3 input sky maps. Zheng et al. (2017a) construct an improved GSM with 5 maps below 408 MHz, and Dowell et al. (2017) use the LWA1 to improve the GSM with their own sky maps. However, the GSM generally suffers from low angular resolution ( $\sim 5^\circ$ ) and systematic errors associated with instrumental artifacts in the input maps. For instance, Dowell et al. (2017) report errors of  $\pm 50\%$  between the GSM and their own maps at 74 MHz, which they attribute to the increasing contribution of free-free absorption and modifications to the synchrotron spectral index at low frequencies.

Widefield interferometric synthesis imaging is a challenging computational problem, and it has been particularly difficult to capture large angular scales  $\gg 10^\circ$  and small angular scales  $\ll 1^\circ$  in a single synthesis image. We will derive a new imaging technique – Tikhonov regularized  $m$ -mode analysis imaging – that allows a drift-scanning interferometer to image the entire visible sky in a single coherent synthesis imaging step with no gridding and no mosaicking.

As a demonstration of this technique we apply Tikhonov regularized  $m$ -mode analysis imaging to the Owens Valley **Radio Observatory** Long Wavelength Array (OVRO-LWA), and generate a series of new low-frequency maps of the sky between 36.528 MHz and 73.152 MHz. These maps capture the full sky visible from the Owens Valley Radio Observatory (OVRO) with angular resolution of  $\sim 15$  arcmin. These new maps complement the existing full-sky maps at these frequencies with greatly improved angular resolution.

We aim for these maps to inform foreground removal strategies in 21-cm cosmology, and we anticipate additional ancillary science taking advantage of the combination of high fidelity and high resolution of these maps, including but not limited to studies of the cosmic ray emissivity at low frequencies, searches for giant radio galaxies, and constraining the galactic synchrotron spectrum. The maps will be made freely available online at the Legacy Archive for Microwave Background Data Analysis (LAMBDA)<sup>1</sup>.

The structure of this paper is as follows. In §2, we present Tikhonov-regularized  $m$ -mode analysis imaging, a new imaging technique that allows us to image the entire visible sky in one coherent synthesis imaging step with exact widefield corrections. In §3 we describe our observations with the **OVRO-LWA**. In §4 we present the sky maps and compare these maps against other low-frequency sky maps. In §5 we discuss some of the sources of error present in the maps, and finally in §6 we present our conclusions.

## 2. ALL-SKY IMAGING

The goal of all imaging algorithms is to estimate the brightness of the sky  $I_\nu(\hat{r})$  in the direction  $\hat{r}$  and frequency  $\nu$ . A radio interferometer measures the visibilities  $V_\nu^{ij,pq}$  between pairs of antennas numbered  $i$  and  $j$  respectively, and between polarizations labeled  $p$  and  $q$  respectively. We will neglect subtleties associated with polarized imaging, so the Stokes- $I$  visibilities are constructed from the sum of the  $pp$  and  $qq$  correlations such that  $V_\nu^{ij} = (V_\nu^{ij,pp} + V_\nu^{ij,qq})/2$ . If the antennas are separated by the baseline  $\vec{b}_{ij}$ , and  $A_\nu(\hat{r})$  describes an antenna's response to the incident Stokes- $I$  radiation (here assumed to be the same for each antenna), then

$$V_\nu^{ij} = \int_{\text{sky}} A_\nu(\hat{r}) I_\nu(\hat{r}) \exp\left(2\pi i \hat{r} \cdot \vec{b}_{ij}/\lambda\right) d\Omega, \quad (2)$$

where the integral runs over solid angle  $\Omega$ . Constructing an image from the output of a radio interferometer

consists of estimating  $I_\nu(\hat{r})$  given the available measurements  $V_\nu^{ij}$ .

For later convenience we will define the baseline transfer function  $B_\nu^{ij}(\hat{r})$  such that

$$V_\nu^{ij} = \int_{\text{sky}} B_\nu^{ij}(\hat{r}) I_\nu(\hat{r}) d\Omega. \quad (3)$$

The baseline transfer function defines the response of a single baseline to the sky, and is a function of the antenna primary beam, and baseline length and orientation.

Naively one might attempt to solve Equation 2 by discretizing, and subsequently solving the resulting matrix equation. If the interferometer is composed of  $N_{\text{base}}$  baselines, and measures  $N_{\text{freq}}$  frequency channels over  $N_{\text{time}}$  integrations, then the entire data set consists of  $N_{\text{base}}N_{\text{freq}}N_{\text{time}}$  complex numbers. If the sky is discretized into  $N_{\text{pix}}$  pixels then the relevant matrix has dimensions of  $(N_{\text{base}}N_{\text{freq}}N_{\text{time}}) \times (N_{\text{pix}})$ . For making single-channel maps with the OVRO-LWA this becomes a 5 petabyte array (assuming each matrix element is a 64-bit complex floating point number). This matrix equation is therefore prohibitively large, and solving Equation 2 by means of discretization is usually intractable, although Zheng et al. (2017b) demonstrate this technique with the MITEOR telescope.

Instead, it is common to make mild assumptions that simplify Equation 2 and ease the computational burden in solving for  $I_\nu(\hat{r})$ . For example, when all of the baselines  $\vec{b}_{ij}$  lie in a plane and the field-of-view is small, Equation 2 can be well-approximated by a two-dimensional Fourier transform (Thompson et al. 2001). The restriction on baseline co-planarity and field-of-view can be relaxed by using W-projection (Cornwell et al. 2008). Known primary beam effects can also be accounted for during imaging by using A-projection (Bhattacharya et al. 2013).

### 2.1. $m$ -Mode Analysis

Transit telescopes can take advantage of a symmetry in Equation 2 that greatly reduces the amount of computer time required to image the full-sky with exact incorporation of widefield imaging effects. This technique, called  $m$ -mode analysis, also obviates the need for gridding and mosaicking. Instead the entire sky is imaged in one coherent synthesis imaging step. We will briefly summarize  $m$ -mode analysis below, but the interested reader should consult Shaw et al. (2014, 2015) for a complete derivation.

In the context of  $m$ -mode analysis, a transit telescope is any interferometer for which the response pattern of the individual elements does not change with respect to

<sup>1</sup> <https://lambda.gsfc.nasa.gov/>

time. This may be an interferometer like the OVRO-LWA where the correlation elements are fixed dipoles, but it may also be an interferometer like LOFAR or the MWA if the steerable beams are held in a fixed position (not necessarily at zenith). The interferometer also does not necessarily have to be homogeneous. Heterogeneous arrays composed of several different types of antennas are allowed as long as care is taken to generalize Equation 2 for a heterogeneous array.

For a transit telescope, the visibilities  $V_\nu^{ij}$  are a periodic function of sidereal time.<sup>2</sup> Therefore it is a natural operation to compute the Fourier transform of the visibilities with respect to sidereal time  $\phi \in [0, 2\pi)$ .

$$V_{m,\nu}^{ij} = \int_0^{2\pi} V_\nu^{ij}(\phi) \exp(-im\phi) d\phi \quad (4)$$

The output of this Fourier transform is the set of  $m$ -modes  $V_{m,\nu}^{ij}$  where  $m = 0, \pm 1, \pm 2, \dots$  is the Fourier conjugate variable to the sidereal time. The  $m$ -mode corresponding to  $m = 0$  is a simple average of the visibilities over sidereal time. Similarly  $m = 1$  corresponds to the component of the visibilities that varies over half-day timescales. Larger values of  $m$  correspond to components that vary on quicker timescales.

Shaw et al. (2014, 2015) show that there is a discrete linear relationship between the measured  $m$ -modes  $V_{m,\nu}^{ij}$ , and the spherical harmonic coefficients of the sky brightness  $a_{lm,\nu}$ .

$$V_{m,\nu}^{ij} = \sum_l B_{lm,\nu}^{ij} a_{lm,\nu}, \quad (5)$$

where the transfer coefficients  $B_{lm,\nu}^{ij}$  are computed from the spherical harmonic transform of the baseline transfer function defined by Equation 3. These transfer coefficients define the interferometer's response to the corresponding spherical harmonic coefficients.

Equation 5 can be recognized as a matrix equation where the transfer matrix  $\mathbf{B}$  is block-diagonal.

$$\underbrace{\begin{pmatrix} v \\ \vdots \\ m\text{-modes} \\ \vdots \end{pmatrix}}_v = \underbrace{\begin{pmatrix} & & & \\ & \ddots & & \\ & & \text{transfer matrix} & \\ & & & \ddots \end{pmatrix}}_B \underbrace{\begin{pmatrix} a \\ \vdots \\ a_{lm} \\ \vdots \end{pmatrix}}_a \quad (6)$$

<sup>2</sup> This is not strictly true. Ionospheric fluctuations and non-sidereal sources (such as the Sun) will violate this assumption. This paper will, however, demonstrate that the impact on the final maps is mild.

$$\mathbf{B} = \begin{pmatrix} m=0 & & & \\ & m=\pm 1 & & \\ & & m=\pm 2 & \\ & & & \ddots \end{pmatrix} \quad (7)$$

The vector  $v$  contains the list of  $m$ -modes and the vector  $a$  contains the list of spherical harmonic coefficients representing the sky brightness. In order to take advantage of the block-diagonal structure in  $\mathbf{B}$ ,  $v$  and  $a$  must be sorted by the absolute value of  $m$ . Positive and negative values of  $m$  are grouped together because the brightness of the sky is real-valued, and the spherical harmonic transform of a real-valued function has  $a_{l(-m)} = (-1)^m a_{lm}^*$ .

In practice, we now need to pick the set of spherical harmonics we will use to represent the sky. For an interferometer like the OVRO-LWA with many short baselines, a sensible choice is to use all spherical harmonics with  $l \leq l_{\max}$  for some  $l_{\max}$ . The parameter  $l_{\max}$  is determined by the maximum baseline length of the interferometer. For an interferometer without short spacings, a minimum value for  $l$  might also be used. This  $l_{\min}$  parameter should be determined by the minimum baseline length. A rough estimate of  $l$  for a baseline of length  $b$  at frequency  $\nu$  is  $l \sim \pi b \nu / c$ . Based on this estimate for the OVRO-LWA and other computational considerations, we therefore adapt  $l_{\min} = 1$  and  $l_{\max} = 1000$  across all frequencies. However, this choice of  $l_{\max}$  actually limits the angular resolution above 55 MHz, and therefore future work will increase  $l_{\max}$  to obtain better angular resolution.

The interferometer's sensitivity to the monopole ( $a_{00}$ ) deserves special consideration. Venumadhav et al. (2016) prove – under fairly general assumptions – that a baseline with nonzero sensitivity to  $a_{00}$  must also have some amount of cross-talk or common-mode noise. In fact the sensitivity to  $a_{00}$  is proportional to a sum of these effects. For example, one way a baseline can have nonzero sensitivity to  $a_{00}$  is if the baseline is extremely short. In this case the antennas are so close together that voltage fluctuations in one antenna can couple into the other antenna. In order to make an interferometric measurement of  $a_{00}$ , this coupling must be measured and calibrated. Consequently, we set  $a_{00} = 0$  in our analysis. In the future this limitation will be addressed with the inclusion of calibrated total power radiometry.

The size of a typical block in the transfer matrix is  $(2N_{\text{base}} N_{\text{freq}}) \times (l_{\max})$ . If each element of the matrix is stored as a 64-bit complex floating point number, a single block is 500 MB for the case of single-channel imag-

ing with the OVRO-LWA, which a modern computer can easily store and manipulate in memory. However, with additional bandwidth these blocks quickly become unwieldy; thus as a first pass, the analysis in this paper is restricted to single-channel imaging. Note also that for the OVRO-LWA  $N_{\text{base}} \gg l_{\max}$ , so there are more measurements than unknowns in Equation 6.

The key advantage of  $m$ -mode analysis is the block-diagonal structure of Equation 6. The computational complexity of many common matrix operations (eg. solving a linear system of equations) is  $\mathcal{O}(N^3)$ , where  **$N$  is the linear size of the matrix. By splitting the equation into  $M$  independent blocks, the number of floating point operations required to solve the linear system of equations is now  $\mathcal{O}(N^3 M^{-2})$ , because each block can be manipulated independently of the other blocks. This computational savings is what makes this matrix algebra approach to interferometric imaging feasible. For the dataset presented in this paper, computing the elements of the transfer matrix takes  $\sim 10$  hours per frequency channel on a 10-node cluster, but once the matrix has been computed the imaging process described in §2.2 takes  $\sim 10$  minutes, and the deconvolution process described in §2.3 was allowed to run for  $\sim 10$  hours.**

## 2.2. *m*-Mode Analysis Imaging

Imaging in  $m$ -mode analysis essentially amounts to inverting Equation 6 to solve for the spherical harmonic coefficients  $\mathbf{a}$ . The linear-least squares solution, which minimizes  $\|\mathbf{v} - \mathbf{B}\mathbf{a}\|^2$ , is given by

$$\hat{\mathbf{a}}_{\text{LLS}} = (\mathbf{B}^* \mathbf{B})^{-1} \mathbf{B}^* \mathbf{v}, \quad (8)$$

where  $*$  indicates the conjugate-transpose.

However, usually one will find that  $\mathbf{B}$  is not full-rank, and hence  $\mathbf{B}^* \mathbf{B}$  is not an invertible matrix. For example, an interferometer located in the northern hemisphere will never see a region of the southern sky centered on the southern celestial pole. The  $m$ -modes contained in the vector  $\mathbf{v}$  must contain no information about the sky around the southern celestial pole, and therefore the act of multiplying by  $\mathbf{B}$  must destroy some information about the sky. The consequence of this fact is that  $\mathbf{B}$  must have at least one singular value that is equal to zero. It then follows that  $\mathbf{B}^* \mathbf{B}$  must have at least one eigenvalue that is equal to zero, which means it is not an invertible matrix.

Another way of looking at the problem is that because the interferometer is not sensitive to part of the southern hemisphere, there are infinitely many possible solutions to Equation 6 that will fit the measured data equally

well. We will therefore regularize the problem and apply an additional constraint that prefers a unique yet physically reasonable solution.

### 2.2.1. Tikhonov Regularization

The process of Tikhonov regularization minimizes  $\|\mathbf{v} - \mathbf{B}\mathbf{a}\|^2 + \varepsilon \|\mathbf{a}\|^2$  for some arbitrary value of  $\varepsilon > 0$  chosen by the observer. The solution that minimizes this expression is given by

$$\hat{\mathbf{a}}_{\text{Tikhonov}} = (\mathbf{B}^* \mathbf{B} + \varepsilon \mathbf{I})^{-1} \mathbf{B}^* \mathbf{v}. \quad (9)$$

Tikhonov regularization adds a small value  $\varepsilon$  to the diagonal of  $\mathbf{B}^* \mathbf{B}$ , fixing the matrix's singularity. By using the singular value decomposition (SVD) of the matrix  $\mathbf{B} = \mathbf{U} \Sigma \mathbf{V}^*$ , Equation 9 becomes

$$\hat{\mathbf{a}}_{\text{Tikhonov}} = \mathbf{V} (\Sigma^2 + \varepsilon \mathbf{I})^{-1} \Sigma \mathbf{U}^* \mathbf{v}, \quad (10)$$

where

$$\Sigma = \begin{pmatrix} \sigma_1 & & \\ & \sigma_2 & \\ & & \ddots \end{pmatrix}.$$

The diagonal elements of  $\Sigma$  are the singular values of  $\mathbf{B}$ . The contribution of each singular component to the Tikhonov-regularized solution is scaled by  $\sigma_i / (\sigma_i^2 + \varepsilon)$ , where  $\sigma_i$  is the singular value for the  $i$ th singular component. Tikhonov regularization therefore acts to suppress any component for which  $\sigma_i \lesssim \sqrt{\varepsilon}$ . If  $\sigma_i = 0$ , the component is set to zero.

In practice the measurement  $\mathbf{v}$  is corrupted by noise with covariance  $\mathbf{N}$ . For illustrative purposes we will assume that  $\mathbf{N} = n \mathbf{I}$  for some  $n > 0$ . In this case, the covariance of the Tikhonov-regularized spherical harmonic coefficients is

$$\mathbf{C} = n \mathbf{V} (\Sigma^2 + \varepsilon \mathbf{I})^{-2} \Sigma^2 \mathbf{V}^*. \quad (11)$$

Each singular component is scaled by a factor of  $\sigma_i^2 / (\sigma_i^2 + \varepsilon)^2$ . In the absence of Tikhonov regularization ( $\varepsilon = 0$ ), singular components with the smallest singular values – the ones that the interferometer is the least sensitive to – actually come to dominate the covariance of the measured spherical harmonic coefficients. Tikhonov regularization improves this situation by downweighting these components.

### 2.2.2. L-Curves

Tikhonov regularization requires the observer to pick the value of  $\varepsilon$ . If  $\varepsilon$  is too large then too much importance is placed on minimizing the norm of the solution and the least-squares residuals will suffer. Conversely, if  $\varepsilon$  is too

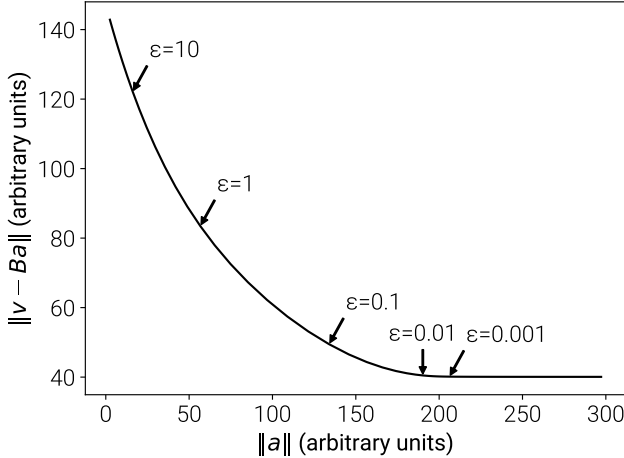


**Figure 1.** An example L-curve computed from OVRO-LWA data at 36.528 MHz by trialing 200 different values of the regularization parameter  $\epsilon$ . The  $x$ -axis is the norm of the solution (in this case the spherical harmonic coefficients) given in arbitrary units, and the  $y$ -axis is the least-squares norm given in arbitrary units. Where the regularization parameter is small, the norm of the solution grows rapidly. Where the regularization parameter is large, the least-squares norm grows rapidly.

small then the problem will be poorly regularized and the resulting sky map may not represent the true sky. Picking the value of  $\epsilon$  therefore requires understanding the trade-off between the two norms.

This trade-off can be analyzed quantitatively by trialing several values of  $\epsilon$ , and computing  $\|\mathbf{v} - \mathbf{B}\mathbf{a}\|^2$  and  $\|\mathbf{a}\|^2$  for each trial. An example is shown in Figure 1. The shape of this curve has a characteristic L-shape, and as a result this type of plot is called an L-curve. The ideal value of  $\epsilon$  lies near the turning point of the plot. At this point a small decrease in  $\epsilon$  will lead to an undesired rapid increase in  $\|\mathbf{a}\|^2$ , and a small increase in  $\epsilon$  will lead to an undesired rapid increase in  $\|\mathbf{v} - \mathbf{B}\mathbf{a}\|^2$ .

In practice, the L-curve should be used as a guide to estimate a reasonable value of  $\epsilon$ . However better results can often be obtained by tuning the value of  $\epsilon$ . For instance, increasing the value of  $\epsilon$  can improve the noise properties of the map by down-weighting noisy modes. Decreasing the value of  $\epsilon$  can improve the resolution of the map by up-weighting the contribution of longer baselines, which are likely fewer in number. In this respect, choosing the value of  $\epsilon$  is analogous to picking the weighting scheme in traditional imaging where robust weighting schemes can be tuned to similar effect (Briggs 1995). For the OVRO-LWA we selected  $\epsilon = 0.01$  across all frequency channels. The distribution of singular values of the transfer matrix with respect to  $\sqrt{\epsilon}$  is summarized in Table 1.

### 2.2.3. Other Regularization Schemes

The choice of applying Tikhonov regularization to  $m$ -mode analysis imaging is not unique. There exists a plethora of alternative regularization schemes that could also be applied. Each regularization scheme has its own advantages and disadvantages. For instance, Tikhonov regularization is simple, independent of prior information, and sets unmeasured modes to zero (a sensible expectation). We will now briefly discuss a few other alternatives.

The Moore-Penrose pseudoinverse (denoted with a superscript  $\dagger$ ), is commonly applied to find the minimum-norm linear-least squares solution to a set of linear equations. This can be used in place of Tikhonov regularization as

$$\hat{\mathbf{a}}_{\text{Moore-Penrose}} = \mathbf{B}^\dagger \mathbf{v}. \quad (12)$$

Much like Tikhonov regularization, the Moore-Penrose pseudoinverse sets components with small singular values (below some user-defined threshold) to zero. Components with large singular values (above the user-defined threshold) are included in the calculation at their full amplitude with no down-weighting of modes near the threshold. The essential difference between using the Moore-Penrose pseudoinverse and Tikhonov regularization is that the pseudoinverse defines a hard transition from “on” to “off”. Modes are either set to zero or included in the map at their full amplitude. On the other hand, Tikhonov regularization smoothly interpolates between these behaviors. Because of this, Tikhonov regularization tends to produce better results in practical applications.

If the measured  $m$ -modes have a noise covariance matrix  $\mathbf{N} \neq n\mathbf{I}$  for some scalar  $n$  (eg. the interferometer is inhomogeneous), then the observer should minimize  $(\mathbf{v} - \mathbf{B}\mathbf{a})^* \mathbf{N}^{-1} (\mathbf{v} - \mathbf{B}\mathbf{a}) + \epsilon \|\mathbf{a}\|^2$ . The noise covariance matrix  $\mathbf{N}$  is used to weight the measurements such that

$$\hat{\mathbf{a}}_{\min \text{ variance}} = (\mathbf{B}^* \mathbf{N}^{-1} \mathbf{B} + \epsilon \mathbf{I})^{-1} \mathbf{B} \mathbf{N}^{-1} \mathbf{v}. \quad (13)$$

In the event that the observer has a prior map of the sky,  $\|\mathbf{a} - \mathbf{a}_{\text{prior}}\|^2$  can be used as the regularizing norm. This will use the prior map to fill-in missing information instead of setting these modes to zero. In this case, the minimum is at

$$\hat{\mathbf{a}}_{\text{with prior}} = (\mathbf{B}^* \mathbf{B} + \epsilon \mathbf{I})^{-1} (\mathbf{B}^* (\mathbf{v} - \mathbf{B}\mathbf{a}_{\text{prior}})) + \mathbf{a}_{\text{prior}}. \quad (14)$$

If instead the observer has a prior expectation on the covariance of the spherical harmonic coefficients, Wiener filtering can also be used. This technique is demonstrated for simulated measurements by Berger et al. (2016).

Alternatively, we could opt to regularize the problem by enforcing smoothness in the sky maps. In this case, the regularizing norm should be of the form  $\|\nabla I(\hat{r})\|^2$ , where  $\nabla I$  is the gradient of the sky brightness in the direction  $\hat{r}$ . This is actually a generalization of Tikhonov regularization where the objective function is  $\|\mathbf{v} - \mathbf{B}\mathbf{a}\|^2 + \varepsilon\|\mathbf{A}\mathbf{a}\|^2$  for some matrix  $\mathbf{A}$ . The minimum is at

$$\hat{\mathbf{a}}_{\text{generalized}} = (\mathbf{B}^*\mathbf{B} + \varepsilon\mathbf{A}^*\mathbf{A})^{-1}\mathbf{B}^*\mathbf{v}. \quad (15)$$

Finally, in many machine learning applications the  $L_1$ -norm<sup>3</sup> is used in place of the usual  $L_2$ -norm in order to encourage sparsity in the reconstructed signal. Applying this to  $m$ -mode analysis imaging would amount to minimizing  $\|\mathbf{v} - \mathbf{B}\mathbf{a}\|_2^2 + \varepsilon\|\mathbf{a}\|_1$ . However, because we have decomposed the sky in terms of spherical harmonics, the vector  $\mathbf{a}$  is not expected to be sparse. Consequently, the  $L_1$ -norm is generally inappropriate for  $m$ -mode analysis imaging without an additional change-of-variables designed to introduce sparsity.

### 2.3. CLEAN

In traditional radio astronomy imaging, CLEAN (Högbom 1974) is a physically motivated algorithm that interpolates between measured visibilities on the  $uv$ -plane. In the absence of this interpolation, gaps in the interferometer's  $uv$ -coverage are assumed to be zero, and – in the image plane – sources are convolved with a point spread function (PSF) that is characteristic of the  $uv$ -coverage. Fundamentally, the interferometer's PSF is determined by which modes were assumed to be zero in the initial imaging process.

In  $m$ -mode analysis imaging, we assumed modes were zero in two separate ways:

1. We selected a set of spherical harmonic coefficients  $a_{lm}$  to describe the sky brightness distribution. All modes with  $l > l_{\max}$  are neglected and assumed to be zero.
2. Tikhonov regularization forces linear combinations of spherical harmonic coefficients with  $\sigma_i \lesssim \sqrt{\varepsilon}$  towards zero.

As a consequence, the final map of the sky is not assembled from a complete set of spherical harmonics. Therefore, just as in traditional imaging,  $m$ -mode analysis imaging produces dirty maps in which sources are convolved with a PSF. This PSF can be improved by increasing the number and variety of baselines, which

<sup>3</sup>  $\|\mathbf{a}\|_1 = \sum_i |a_i|$

increases the number of modes for which  $\sigma_i \gg \sqrt{\varepsilon}$ . Alternatively, by collecting more data, the signal-noise ratio of the measured  $m$ -modes increases, which allows the observer to lower the value of  $\varepsilon$  without increasing the noise in the maps. Finally, the CLEAN algorithm can be applied to interpolate some of the missing information that was assumed to be zero.

The PSF of a dirty  $m$ -mode analysis map may be computed with

$$\mathbf{a}_{\text{PSF}}(\theta, \phi) = (\mathbf{B}^*\mathbf{B} + \varepsilon\mathbf{I})^{-1}\mathbf{B}^*\mathbf{B}\mathbf{a}_{\text{PS}}(\theta, \phi), \quad (16)$$

where  $\mathbf{a}_{\text{PSF}}(\theta, \phi)$  is the vector of spherical harmonic coefficients representing the PSF at the spherical coordinates  $(\theta, \phi)$ , and  $\mathbf{a}_{\text{PS}}(\theta, \phi)$  is the vector of spherical harmonic coefficients for a point source at  $(\theta, \phi)$  given by

$$\mathbf{a}_{\text{PS}}(\theta, \phi) = \begin{pmatrix} \vdots \\ Y_{lm}^*(\theta, \phi) \\ \vdots \end{pmatrix} = \begin{pmatrix} \vdots \\ Y_{lm}^*(\theta, 0) \times e^{im\phi} \\ \vdots \end{pmatrix}. \quad (17)$$

In general, the PSF can be a function of the right ascension and declination. However, point sources at the same declination take the same track through the sky and (barring any ionospheric effects) will have the same PSF. The PSF is therefore only a function of the declination. For example, sources at low elevations will tend to have an extended PSF along the north-south axis due to baseline foreshortening. For the OVRO-LWA antenna configuration (Figure 2), example PSFs at three separate frequencies are shown in Figure 3. Adapting CLEAN for  $m$ -mode analysis requires either pre-computing Equation 16 at a grid of declinations, or a method for rapidly evaluating Equation 16 on the fly.

For an interferometer with more baselines than spherical harmonics used in the maps (eg. the OVRO-LWA),  $\mathbf{B}^*\mathbf{B}$  can be a much smaller matrix than the full transfer matrix  $\mathbf{B}$ . Therefore pre-computing  $\mathbf{B}^*\mathbf{B}$  can allow the entire matrix to fit into memory on a single machine. This greatly reduces the amount of disk I/O necessary for solving Equation 16.

Additionally, we can pre-compute the Cholesky decomposition of  $\mathbf{B}^*\mathbf{B} + \varepsilon\mathbf{I} = \mathbf{U}^*\mathbf{U}$ , where  $\mathbf{U}$  is an upper-triangular matrix. Inverting an upper triangular matrix is an  $\mathcal{O}(N^2)$  operation (instead of  $\mathcal{O}(N^3)$  for a general matrix inverse).<sup>4</sup> Equation 16 can then be rapidly eval-

<sup>4</sup> Instead of computing  $\mathbf{A}^{-1}$ , we solve the linear equation  $\mathbf{Ax} = \mathbf{b}$  each time the matrix inverse is needed so as to avoid numerical instabilities.

uated from right to left as:

$$\mathbf{a}_{\text{PSF}} = \mathbf{U}^{-1} (\mathbf{U}^*)^{-1} (\mathbf{B}^* \mathbf{B}) \mathbf{a}_{\text{PS}}. \quad (18)$$

Furthermore, Equation 18 does not need to be separately evaluated for each CLEAN component. Instead we can identify  $N$  CLEAN components, accumulate  $\mathbf{a}_{\text{PS}}$  for each component, and evaluate Equation 18 on the accumulation. This can greatly reduce the number of times this equation needs to be evaluated, but care must be taken to ensure that the  $N$  components are not so close together that sidelobes from one may interact with another.

Altogether the adaptation of CLEAN applied to the maps presented in this paper is summarized below.

**Precondition:**  $\mathbf{a}$  is the solution to Equation 9

```

1: function CLEAN( $\mathbf{a}$ )
2:    $\mathbf{M} \leftarrow \mathbf{B}^* \mathbf{B}$ 
3:    $\mathbf{U} \leftarrow \text{chol}(\mathbf{M} + \varepsilon \mathbf{I})$   $\triangleright$  Cholesky decomposition
4:   while noise in map > threshold do
5:     find  $N$  pixels with the largest residual flux
6:      $\mathbf{x} \leftarrow \sum_{i=1}^N (\text{pixel flux}) \times \mathbf{a}_{\text{PS}}(\theta_i, \phi_i)$ 
7:      $\mathbf{y} \leftarrow \mathbf{U}^{-1} (\mathbf{U}^*)^{-1} \mathbf{M} \mathbf{x}$ 
8:      $\mathbf{a} \leftarrow \mathbf{a} - (\text{loop gain}) \times \mathbf{y}$ 
9:     record subtracted components
10:     $\mathbf{a} \leftarrow \mathbf{a} + (\text{restored components})$ 
11:   return  $\mathbf{a}$ 
```

In summary, Tikhonov-regularized  $m$ -mode analysis imaging constructs a widefield synthesis image of the sky from a complete earth rotation, and with exact treatment of widefield-effects. This is accomplished by solving a regularized block-diagonal matrix equation (Equation 9). The solution to this equation generates a map where sources are convolved with a PSF characteristic of the interferometer (a function of the frequency, antenna response, and baseline distribution with a full Earth rotation). The CLEAN algorithm is adopted to deconvolve the PSF and produce the final sky maps.

### 3. OBSERVATIONS

#### 3.1. The Owens Valley **Radio Observatory** Long Wavelength Array

The Owens Valley **Radio Observatory** Long Wavelength Array (OVRO-LWA) is a 288-element interferometer located at the Owens Valley Radio Observatory near Big Pine, California (Hallinan et al. in prep.). The OVRO-LWA is a low-frequency instrument with instantaneous bandwidth covering 27 MHz to 85 MHz and with 24 kHz channelization. Each antenna stand hosts two perpendicular broadband dipoles so that there are  $288 \times 2$  signal paths in total. These signal paths feed into the 512-input LEDA correlator (Kocz et al. 2015),

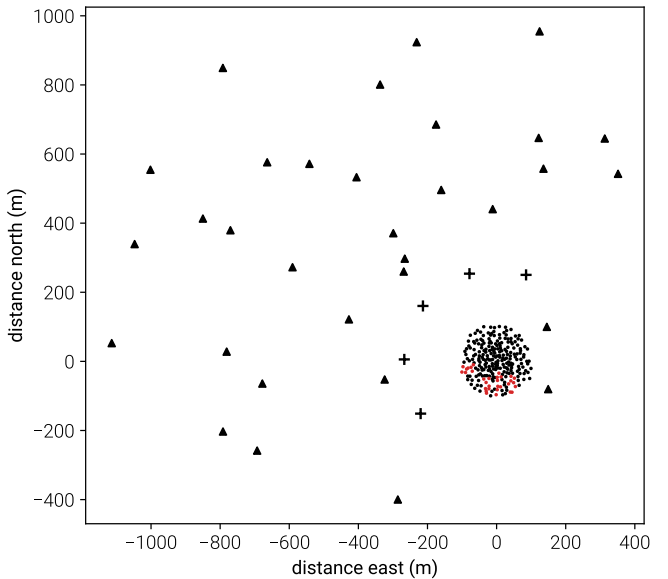


**Figure 2.** Antenna layout for the OVRO-LWA. Black dots correspond to antennas within the 200 m diameter core of the array. The 32 triangles are the expansion antennas built in early 2016 in order to increase the longest baseline to  $\sim 1.5$  km. The red dots are core antennas that are disconnected from the correlator in order to accommodate these antennas. The 5 crosses are antennas equipped with noise-switched front ends.

which allows the OVRO-LWA to capture the entire visible hemisphere in a single snapshot image.

The 288 antennas are arranged in a pseudo-random configuration optimized to minimize sidelobes in snapshot imaging (see Figure 2). Of these 288 antennas, 251 are contained within a 200 m diameter core, 32 are placed outside of the core in order to extend the maximum baseline length to  $\sim 1.5$  km, and the final 5 antennas are equipped with noise-switched front ends for calibrated total power measurements of the global sky brightness. These antennas are used as part of the LEDA experiment (Price et al. 2017) to measure the global signal of 21-cm absorption from the cosmic dawn. In the current configuration, 32 antennas (64 signal paths) from the core are disconnected from the correlator in order to accommodate the 32 antennas on longer baselines. A final stage of construction will involve 64 additional antennas installed on long baselines out to a maximum length of 2.6 km.

The dataset used in this paper spans 28 consecutive hours beginning at 2017-02-17 12:00:00 UTC time. During this time the OVRO-LWA operated as a zenith-pointing drift scanning interferometer. The correlator dump time was selected to be 13 seconds such that the correlator output evenly divides a sidereal day. Due to the computational considerations presented in §2.1,

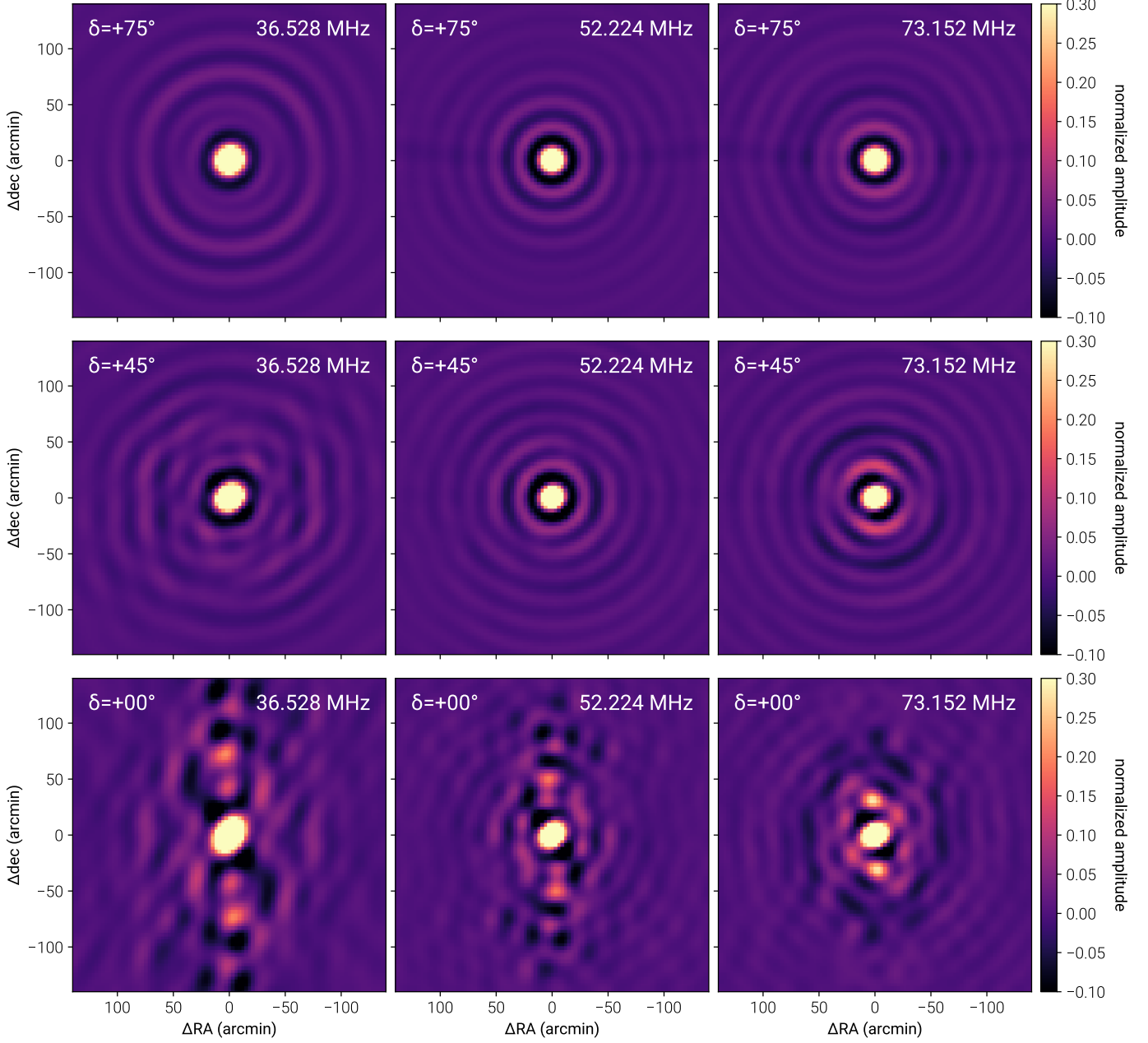


**Figure 3.** The  $m$ -mode analysis imaging PSF at three declinations (top row:  $\delta = +75^\circ$ , middle row:  $\delta = +45^\circ$ , bottom row:  $\delta = +0^\circ$ ) and three frequencies (left column: 36.528 MHz, middle column: 52.224 MHz, right column: 73.152 MHz). The PSF is computed by evaluating Equation 16. Above 55 MHz, the angular extent of the PSF does not follow the expected scaling with frequency because the angular resolution is limited by the selection of  $l_{\max} = 1000$ . The FWHM at  $\delta = +45^\circ$  is listed in Table 1.

eight 24 kHz channels are selected for imaging from this dataset: 36.528 MHz, 41.760 MHz, 46.992 MHz, 52.224 MHz, 57.456 MHz, 62.688 MHz, 67.920 MHz, and 73.152 MHz. These particular channels are chosen due to their location at the exact center of instrumental subbands.

### 3.2. Complex Gain Calibration

The complex gain calibration is responsible for correcting per-antenna amplitude and phase errors. This is accomplished using a sky model and a variant of alternating least squares colloquially known as “Stefcal” (Mitchell et al. 2008; Salvini & Wijnholds 2014)<sup>5</sup>.

<sup>5</sup> The calibration routine is written in the Julia programming language (Bezanson et al. 2017), and is publicly available on-

Cyg A and Cas A are – by an order of magnitude – the brightest point-like radio sources in the northern hemisphere at resolutions lower than  $0.25^\circ$ . Therefore, the optimal time to solve for the interferometer’s gain calibration is when these sources are at high elevations. The antenna complex gains are measured from a 22 minute track of data when Cyg A and Cas A are at high elevations. The gains measured in this way are then used to calibrate the entire 28 hour dataset. The calibration sky model consists only of Cyg A and Cas A. The model flux of Cyg A is set to the Baars et al. (1977) spectrum while the flux of Cas A is measured from the data itself (using a preliminary calibration solved for with a fiducial Cas A spectrum).

Calibrating in this manner generates  $\sim$  arcminute errors in the astrometry of the final sky maps due to ionospheric refractive offsets during the time of calibration. These residual errors in the astrometry are corrected post-imaging by registering the images with respect to all VLSSr (Lane et al. 2014) sources that are bright ( $> 30$  Jy with a consistent flux density measured with the OVRO-LWA), and not too close to other bright sources (at least  $1^\circ$  separation).

Temperature fluctuations of the analog electronics generate 0.1 dB sawtooth oscillations in the analog gain. These oscillations occur with a variable 15 to 17 minute period associated with HVAC cooling cycles within the electronics shelter that houses these electronics. The amplitude of these gain fluctuations is calibrated by smoothing the autocorrelation amplitudes on 45 minute timescales. The ratio of the measured auto-correlation power to the smoothed auto-correlation power defines a per-antenna amplitude correction that is then applied to the cross-correlations. Additionally, the ambient temperature at the front-end electronics (located in a box at the top of each dipole) fluctuates diurnally, which will generate diurnal gain fluctuations. At this time, no correction is made for these diurnal gain fluctuations.

### 3.3. Primary Beam Measurements

In order to generate wide-field images of the sky, the response of the antenna to the sky must be known. Drift-scanning interferometers like the OVRO-LWA can empirically measure their primary beam under a mild set of symmetry assumptions (Pober et al. 2012). The symmetry assumptions are necessary to break the degeneracy between source flux and beam amplitude when the flux of the source is unknown. In this work, we assume symmetries that are apparent in the antenna de-

sign, but real-world defects and coupling with nearby antennas will contribute towards breaking these symmetries at some level. In particular we assume that the  $x$ - and  $y$ -dipoles have the same response to the sky after rotating one by  $90^\circ$ , and that the beam is invariant under north-south and east-west flips.

We measure the flux of several bright sources (Cyg A, Cas A, Tau A, Vir A, Her A, Hya A, 3C 123, and 3C 353) as they pass through the sky, and then fit a beam model composed of Zernike polynomials to those flux measurements. We select the basis functions to have the desired symmetry ( $Z_0^0$ ,  $Z_2^0$ ,  $Z_4^0$ ,  $Z_4^4$ ,  $Z_6^0$ ,  $Z_6^4$ ,  $Z_8^0$ ,  $Z_8^4$ , and  $Z_8^8$ ) and the beam amplitude at zenith is constrained to be unity. See Figure 4 for an illustration of a fitted beam model at several frequencies. This process is repeated for each frequency channel. Residuals for Cyg A and Cas A can be seen in Figure 5.

### 3.4. Ionospheric Conditions

The geomagnetic conditions during this time were mild. The Disturbance storm time (Dst) index, which measures the  $z$ -component of the interplanetary magnetic field, was  $> -30$  nT during the entirety of the observing period.<sup>6</sup> Following the classification scheme of Kintner et al. (2008), a weak geomagnetic storm has  $Dst < -30$  nT. Stronger geomagnetic storms have  $Dst < -50$  nT.

Despite the mild conditions, low frequency interferometric observations are still affected by the index of refraction in the ionosphere. Figure 6 shows the median vertical total electron content (TEC) above OVRO measured from GPS (Iijima et al. 1999). The median is computed over all GPS measurements within 200 km of the observatory. Over the observing period, the TEC smoothly varies from 20 TECU at midday to 5 TECU during the night. However, this measurement is only sensitive to large scale fluctuations in the ionosphere and does not capture small scale fluctuations.

Small scale fluctuations are best characterized by source scintillation and refractive offsets. Figure 5 shows the apparent flux and position offset of Cyg A and Cas A as a function of time over the entire observing period. Both sources exhibit rapid scintillation on the timescale of a single integration (13 seconds). For example, at 36.528 MHz, it is not unusual for Cyg A to have measured flux variations of 50% between adjacent 13 second integrations. The variance at 36.528 MHz compared with the variance at 73.152 MHz is consistent with

line (<https://github.com/mweastwood/TTCal.jl>) under an open source license (GPLv3 or any later version).

<sup>6</sup> The Dst index was obtained from the World Data Center for Geomagnetism, Kyoto University (<http://swdcwww.kugi.kyoto-u.ac.jp/>). Accessed 2017-07-25.

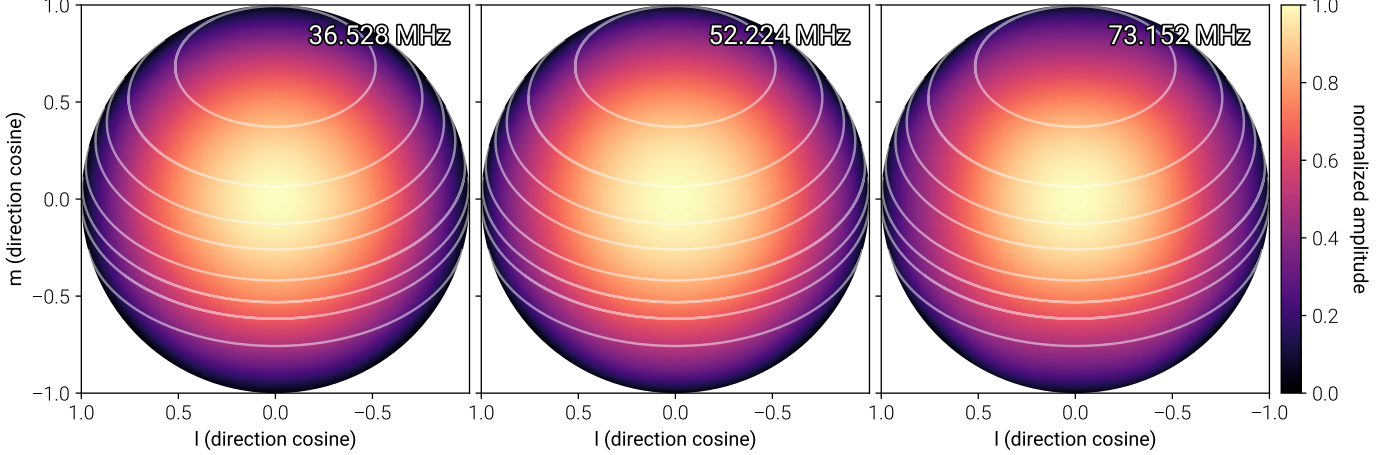


**Figure 4.** Empirical fits to the OVRO-LWA Stokes-I primary beam (the response of the  $x$ - and  $y$ -dipoles has been summed) at three frequencies: 36.528 MHz (left panel), 52.224 MHz (middle panel), and 73.152 MHz (right panel). The source tracks used to measure the beam model are overlaid. From north to south, these tracks correspond to Cas A, Cyg A, 3C 123, Tau A, Vir A, Her A, 3C 353, and Hya A. The fitting process is described in §3.3, and residuals for Cyg A and Cas A are in Figure 5.

an ionospheric  $\nu^{-2}$  origin. The measured position offset of each source is a measurement of the ionospheric phase gradient across the array. This varies on slower 10 minute timescales, with each source refracting by as much as 20 arcmin (at 36.528 MHz) from their true astronomical positions as waves in the ionosphere pass through the line of sight. At 74 MHz on the VLA, Kasim et al. (2007) observe  $\sim 1$  arcmin refractive offsets during the night, and  $\sim 4$  arcmin offsets during the day on similar  $\sim 10$  minute timescales, which is consistent with what is seen here. The impact of these effects on the sky maps is simulated in §5.1.

### 3.5. Source Removal

#### 3.5.1. Cygnus A and Cassiopeia A

Due to the rapid and large ionospheric fluctuations seen in Figure 5, CLEAN cannot be relied on to accurately deconvolve bright sources. However, without removing bright sources from the data, sidelobes from these sources will dominate the variance in the sky maps. At 74 MHz Cyg A is a 15,000 Jy source (Baars et al. 1977). A conservative estimate for the confusion limit at 74 MHz with a 15 arcmin beam is 1000 mJy (Lane et al. 2014). Therefore, we require that Cyg A’s sidelobes be at least  $-45$  dB down from the main lobe to prevent Cyg A’s sidelobes from dominating the variance in the image.

To achieve this dynamic range at low frequencies, it is important to account for propagation effects through the ionosphere. In the weak scattering regime ( $r_{\text{diff}} \gg r_f$ , where  $r_{\text{diff}}$  is the diffractive scale of the ionosphere,  $r_f = \sqrt{\lambda D / 2\pi}$  is the Fresnel scale,  $\lambda$  is the wavelength, and  $D$  is the distance to the ionosphere), fluctua-

tions within the ionosphere contribute amplitude and phase scintillations that can be described by a direction-dependent complex-gain calibration. This justifies the use of “peeling”, which incorporates a direction-dependent calibration to subtract sources in the presence of ionospheric scintillation. (eg. Mitchell et al. 2008; Smirnov & Tasse 2015).

In the strong scattering regime ( $r_{\text{diff}} \lesssim r_f$ ), the image of a point source can “break apart” into multiple images or speckles (Vedantham & Koopmans 2015). Attempting to peel a source in the strong scattering regime will lead to source subtraction artifacts in the final sky map. Mevius et al. (2016) measured that from the location of LOFAR at 150 MHz, the diffractive scale of the ionosphere is  $> 5$  km 90% of the time. This implies that at 73 MHz, the diffractive scale is typically  $> 2$  km, and at 36 MHz, the diffractive scale is typically  $> 1$  km. These limits are comparable to the Fresnel scale for the OVRO-LWA (ie.  $r_{\text{diff}} > r_f$ ), and therefore we do not generally expect to see strong scattering from the ionosphere. Ionospheric conditions during the observing period were mild (see §3.4). However, we do observe scintillation and refractive-offset events on the timescale of a single integration (13 seconds, see Figure 5). Consequently we peeled Cyg A and Cas A from the dataset using a new solution for each integration.

In addition, the largest angular scale of Cas A is  $\sim 8$  arcmin, and the largest angular scale of Cyg A is  $\sim 2$  arcmin. With a  $\sim 10$  arcmin resolution on its longest baselines at 73 MHz, the

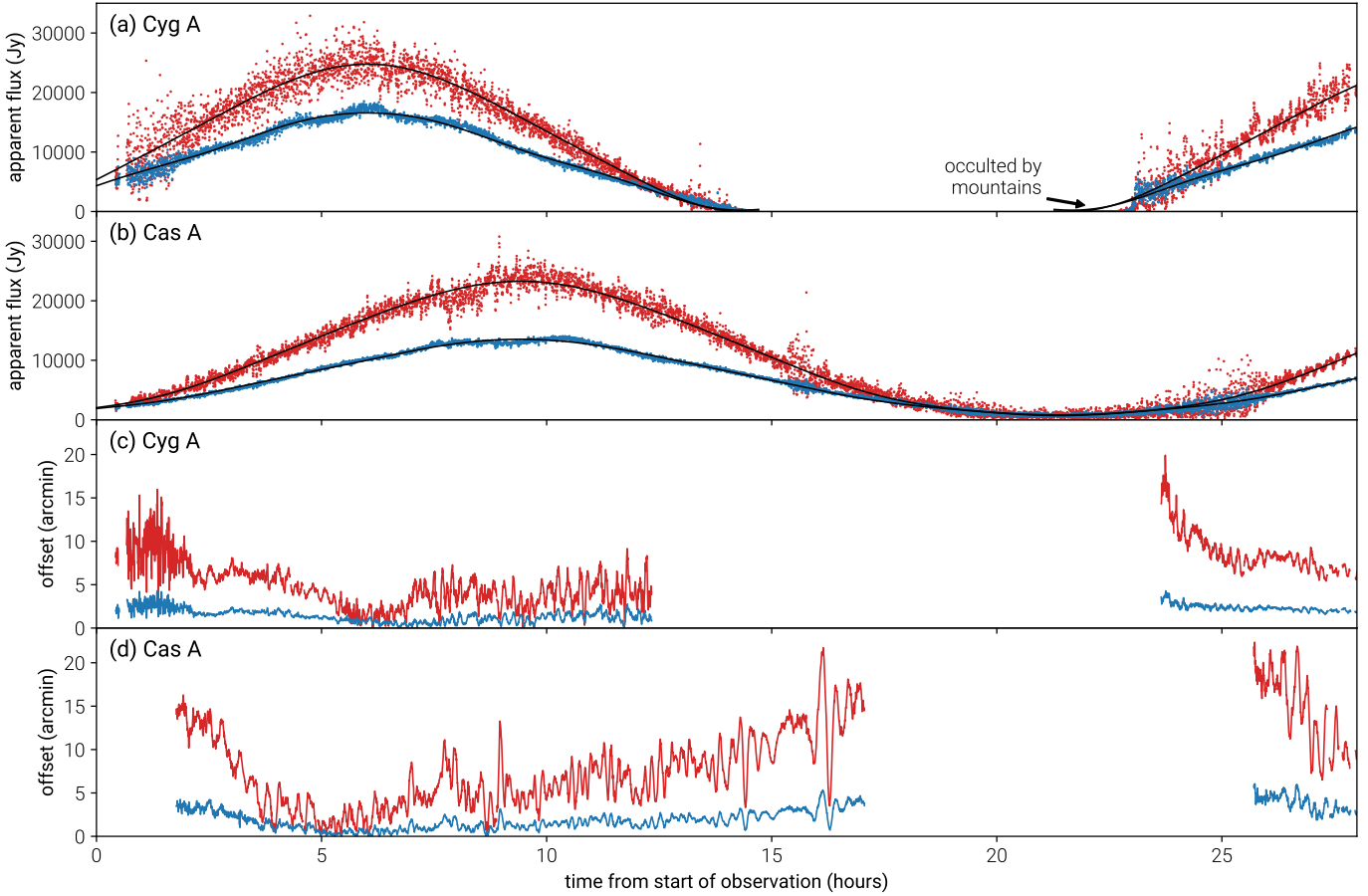


**Figure 5.** Panels (a) and (b) show the measured apparent flux of Cyg A and Cas A at 36.528 MHz (red points) and 73.152 MHz (blue points) as a function of time over the observing period. The solid black curves show the expected flux computed using the empirical beam model fits. The thermal noise contribution to each point is about 50 Jy. Cyg A is occulted by the White Mountains when it is low on the horizon to the east. Panels (c) and (d) show the measured position offset of Cyg A and Cas A relative to their true astronomical positions at 36.528 MHz (red line) and 73.152 MHz (blue line).

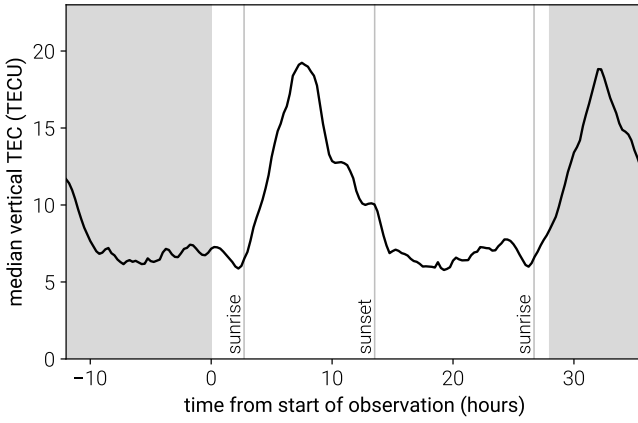


**Figure 6.** The median vertical TEC within 200 km of OVRO during the time of the observation. The gray shaded regions indicate times outside of the observing period. The gray vertical lines indicate sunrise and sunset (as labeled).

OVRO-LWA marginally resolves both sources. A resolved source model is needed for both sources.

We fit a self-consistent resolved source model to each source. This is performed by minimizing the variance within an aperture located on each source after peeling. By phasing up a large number of integrations before imaging (at least 1 hour), it is possible to smear out the contribution of the rest of the sky. We then use a non-linear optimization routine (NLopt Sbplx) (Johnson 2008; Rowan 1990) to vary the parameters in a source model until the variance within the aperture is minimized. Cyg A is modeled with 2 Gaussian components, while Cas A is modeled with 3 Gaussian components. Ultimately, these multi-component models are used to peel Cyg A and Cas A, but residual errors from this model and from the ionosphere (particularly while these sources are at low elevations) contribute residual artifacts that are largely localized to within  $1^\circ$  of each source.

### 3.5.2. Other Bright Sources

Other bright sources – namely Vir A, Tau A, Her A, Hya A, 3C 123, and 3C 353 – are also removed from the visibilities prior to imaging. Because these sources are much fainter than Cyg A and Cas A, we do not need resolved source models to be able to remove these sources from the visibilities without residual sidelobes contaminating the image.

However, the ionosphere will cause these sources to scintillate and refract. The position and flux of each source is measured separately in each channel and integration. The sources are then subtracted from the visibilities using the updated position and flux of the source. The brightest of these sources (Vir A and Tau A) are peeled using a direction dependent calibration when they are at high elevations.

### 3.5.3. The Sun

The Sun can be trivially removed from any map of the sky by constructing the map using only data collected at night. A map of the entire sky can be obtained by using observations spaced 6 months apart. However the dataset used in this paper consists of 28 consecutive hours. Fortunately the Sun was not active during this period, which could have greatly increased the difficulty involved in subtracting the Sun.

We attempt to subtract the Sun from the dataset with the goal of suppressing its sidelobes. The Sun is well-resolved by the OVRO-LWA and hence a detailed source model is needed. In fact, the optical depth  $\tau = 1$  surface of the Sun changes with frequency, and as a consequence a new model is needed at each frequency. While we could fit a limited number of Gaussian components to Cyg A and Cas A, this is insufficient for the Sun. Additionally, while most astronomical sources at these frequencies have negative spectral indices, the Sun has a positive spectral index. Therefore, more care will need to be taken in subtracting the Sun at higher frequencies than at lower frequencies.

The strategy used for removing the Sun below 55 MHz involves fitting a shapelet (Refregier 2003) model to the Sun and subtracting without the use of direction dependent gains. The shapelet fitting is performed in the visibility space. Above 55 MHz a model is fit to the Sun by minimizing the residuals after peeling (in the same way that models are obtained for Cyg A and Cas A). The Sun is then peeled from each integration using direction dependent gains.

## 3.6. Flux Scale

The flux scale of the data was tied to the Baars et al. (1977) spectrum of Cyg A during gain calibra-

tion. However, gain calibration is also a function of the beam model and the spectrum used for Cas A. Recent work by Scaife & Heald (2012) (hereafter SH12) using archival data from the literature and Perley & Butler (2017) (hereafter PB17) using the VLA has expanded the number of low-frequency radio sources with calibrated flux measurements from one (Cyg A) to eleven in total. While the SH12 flux scale is valid between 30 MHz and 300 MHz, the PB17 flux scale is somewhat more limited because the lowest frequency observations come from the VLA 4-band system. As a consequence, the PB17 flux scale is not valid below 50 MHz.

Figure 7 shows a comparison between flux measurements made using the all-sky maps from this work, and spectra from the aforementioned flux scales. Generally the OVRO-LWA flux measurements agree to between 5 and 10% of the SH12 spectra. Below 50 MHz there can be substantial departures with respect to the extrapolated PB17 spectra (for eg. 3C 286, 3C 295, and 3C 380), but it is usually the case that we have much better agreement with the SH12 spectra. This indicates that the PB17 spectra cannot be extrapolated below 50 MHz.

## 4. RESULTS

We constructed eight sky maps using Tikhonov-regularized  $m$ -mode analysis imaging and CLEANing with observations from the OVRO-LWA. Each map is individually shown in Figure 8, Figure 9 is a three-color image constructed from the maps at 36.528 MHz, 52.224 MHz, and 73.152 MHz, and Figure 10 is a cutout of the galactic plane. The maps cover the sky north of  $\delta = -30^\circ$  with  $\sim 15$  arcmin angular resolution. The eight brightest northern hemisphere point sources are removed from each map (Cyg A, Cas A, Vir A, Tau A, Her A, Hya A, 3C 123, and 3C 353) as described in §3.5, and there is a small blank region near  $l = +45.7^\circ$ ,  $b = -47.9^\circ$  corresponding to the position of the Sun during the observing window. The properties of each map – including frequency, bandwidth, angular resolution, and thermal noise – are presented in Table 1.

Each map from Figure 8 will be made freely available online in Healpix format (Górski et al. 2005) on LAMBDA (<https://lambda.gsfc.nasa.gov/>).

Due to the considerations presented by Venumadhav et al. (2016) and discussed in §2.1, each of these maps is monopole subtracted ( $a_{00} = 0$ ). Furthermore, in order to suppress sources of terrestrial interference, all spherical harmonics with  $m = 0$ , or  $m = 1$  and  $l > 100$  are filtered from the map (where the spherical harmonics are defined in the J2017 coordinate system). As will be discussed in §5.4, these spherical harmonics are particu-

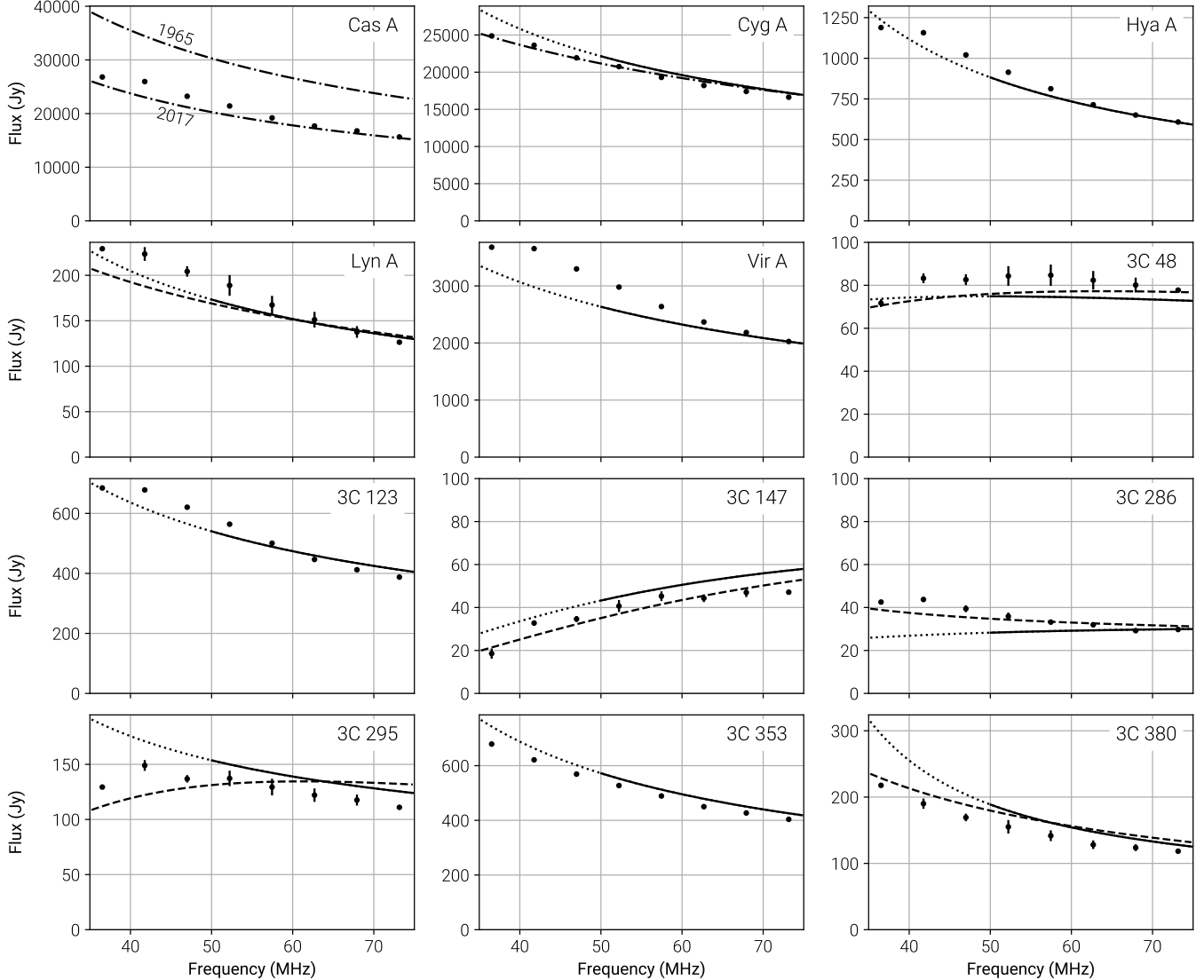


**Figure 7.** Measured fluxes (black points) of 11 sources plotted against the published spectra from Perley & Butler (2017) (solid line above 50 MHz, dotted line below 50 MHz), Scaife & Heald (2012) (dashed line), and Baars et al. (1977) (dot-dash line). Cas A is compared against a spectrum assuming a secular decrease of 0.77% per year (Helmboldt & Kassim 2009).

larly susceptible to contamination by RFI and common-mode pickup. As a consequence, astronomical emission that circles the J2017 north celestial pole (NCP) is filtered from the maps. This filtering creates negative rings around the NCP at the declination of bright point sources. These rings are naturally removed from the map during CLEANing as long as this filtering step is included in the PSF calculation.

The noise in each map is empirically measured using jackknife resampling. The dataset is first split into even- and odd-numbered integrations. These two groups are then imaged and CLEANed independently, before being compared against the maps constructed from all of the available data using the jackknife **standard error** estimator. This estimate of the **standard error** includes all

sources of error that operate on  $\sim 13$  second timescales (the integration time) such as thermal noise and rapid ionospheric fluctuations, but does not account for more slowly varying effects (for example, sidereal variation in the system temperature or day-night fluctuations in the ionosphere). These noise calculations are summarized in Table 1. VLSR source counts (Lane et al. 2014) suggest that the confusion limit at 74 MHz and 15 arcmin angular resolution is  $\sim 1000 \times (\nu/74\text{ MHz})^{-0.7}$  mJy. Each channel map achieves thermal noise  $< 900$  mJy and therefore each map is likely at or near the confusion limit.

In the absence of a zero-level correction, a pixel-by-pixel power law fit to the new maps is impossible. In general this zero-level correction requires calibrated to-

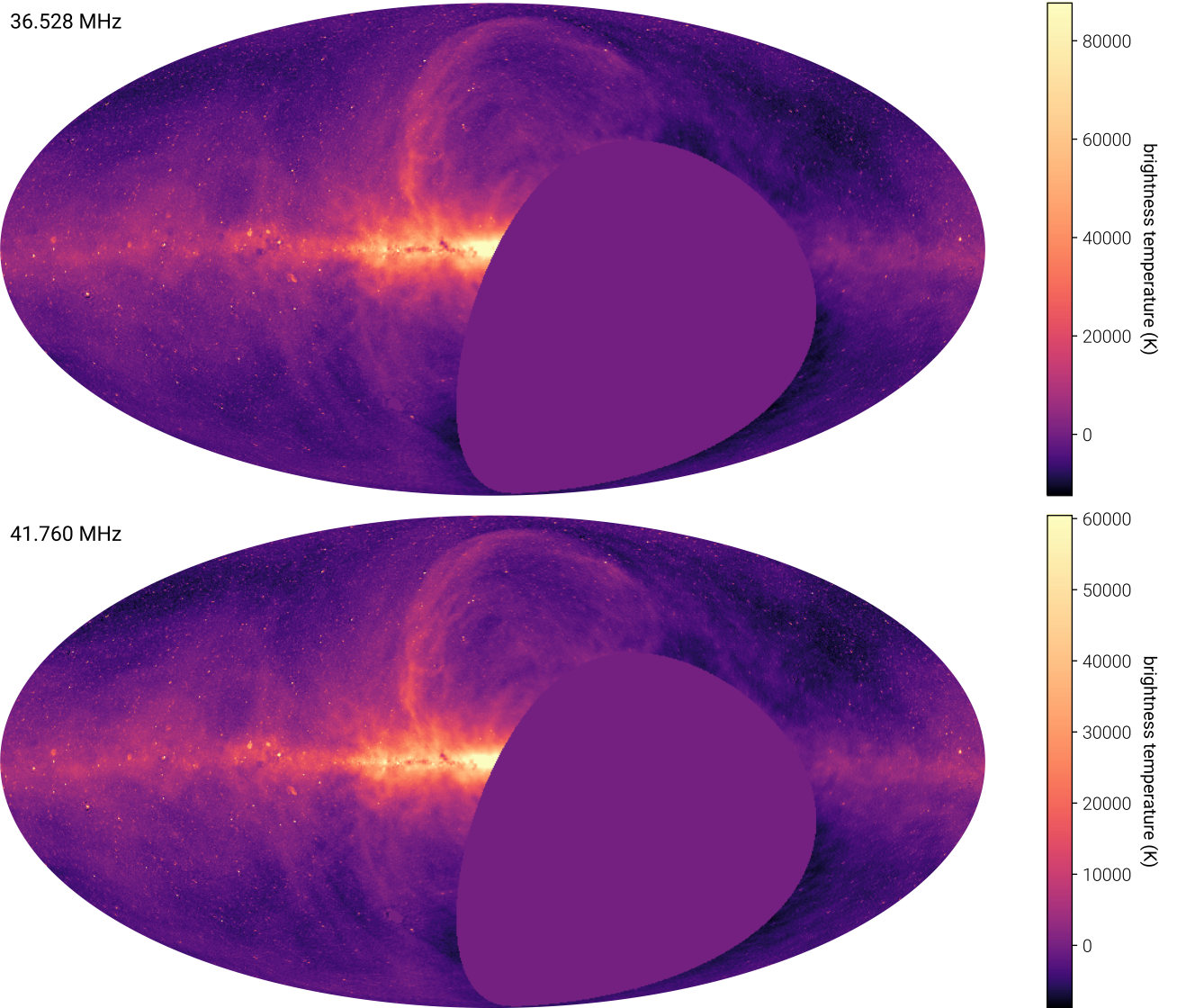


**Figure 8.** These eight panels illustrate (with a Mollweide projection and logarithmic color scale) the eight full-sky maps generated with Tikhonov-regularized  $m$ -mode analysis imaging and the OVRO-LWA. Each map covers the sky north of  $\delta = -30^\circ$  with angular resolution of  $\sim 15$  arcmin. Eight bright sources have been removed from each map (Cyg A, Cas A, Vir A, Tau A, Her A, Hya A, 3C 123, and 3C 353). The small blank region near  $l = +45.7^\circ$ ,  $b = -47.9^\circ$  corresponds to the location of the Sun during the observation period. A detailed summary of the properties of each map is given in Table 1.

tal power measurements that will be included in future work. Instead, temperature-temperature plots (T-T plots) can be used to measure the spectral index independently of any zero-level corrections (Turtle et al. 1962). This method relies on the assumption that all pixels in a given region are described by the same power law. In that case, there exists a linear relationship between the brightness temperature at frequency  $\nu_1$  and frequency  $\nu_2$ . The slope of this best-fit line is a measure of the spectral index between the two frequencies. T-T plots can fail to obtain a reliable measure of the spectral index in two ways. First, if there is not enough dynamic range in the emission region there may be only

a weak correlation between the brightness temperature at  $\nu_1$  and  $\nu_2$ . Second, if two emission mechanisms operate in close proximity (ie. synchrotron and free-free), then a single power-law interpretation of the emission in that region will be poor. Consequently, spectral indices estimated from T-T plots can require careful interpretation.

In Figure 11, the spectral index is locally estimated in each part of the sky within a region  $\sim 10^\circ$  across by constructing local T-T plots between 36.528 MHz and 73.152 MHz. Contours of constant  $R^2$  (the coefficient-of-determination) are overlaid. If  $R^2 \sim 1$ , the spectral index is reliable because there is locally a strong lin-

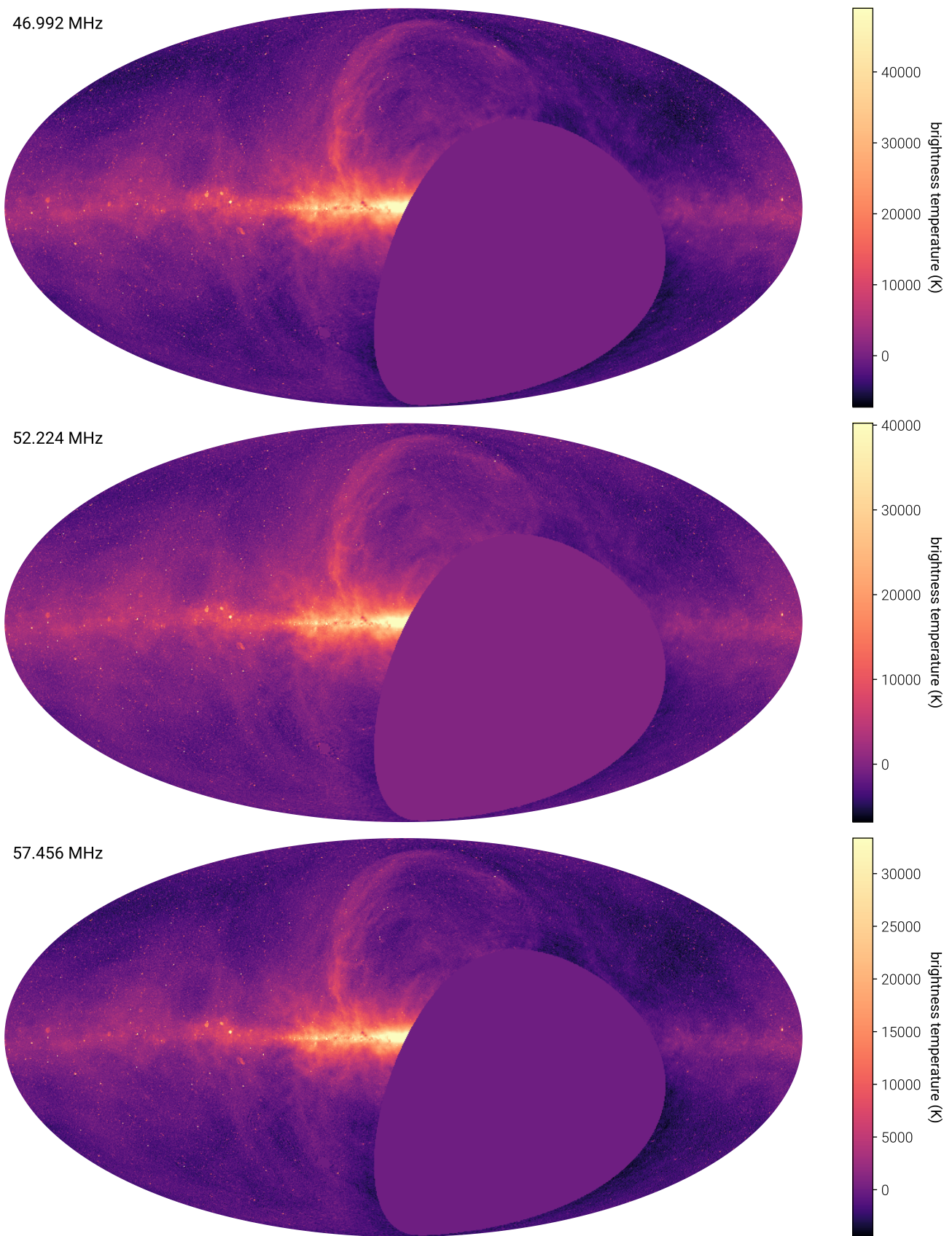


**Figure 8.** continued

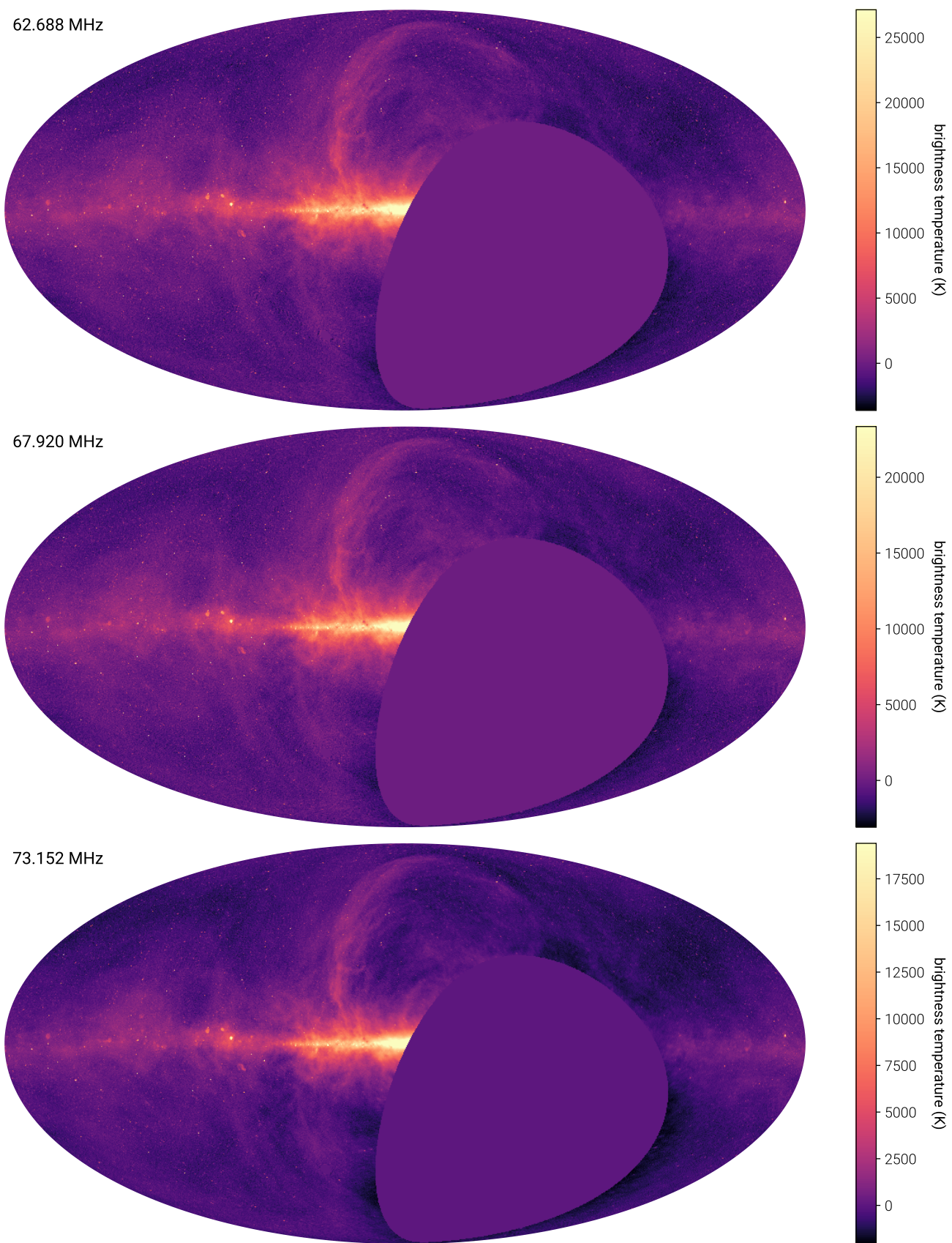
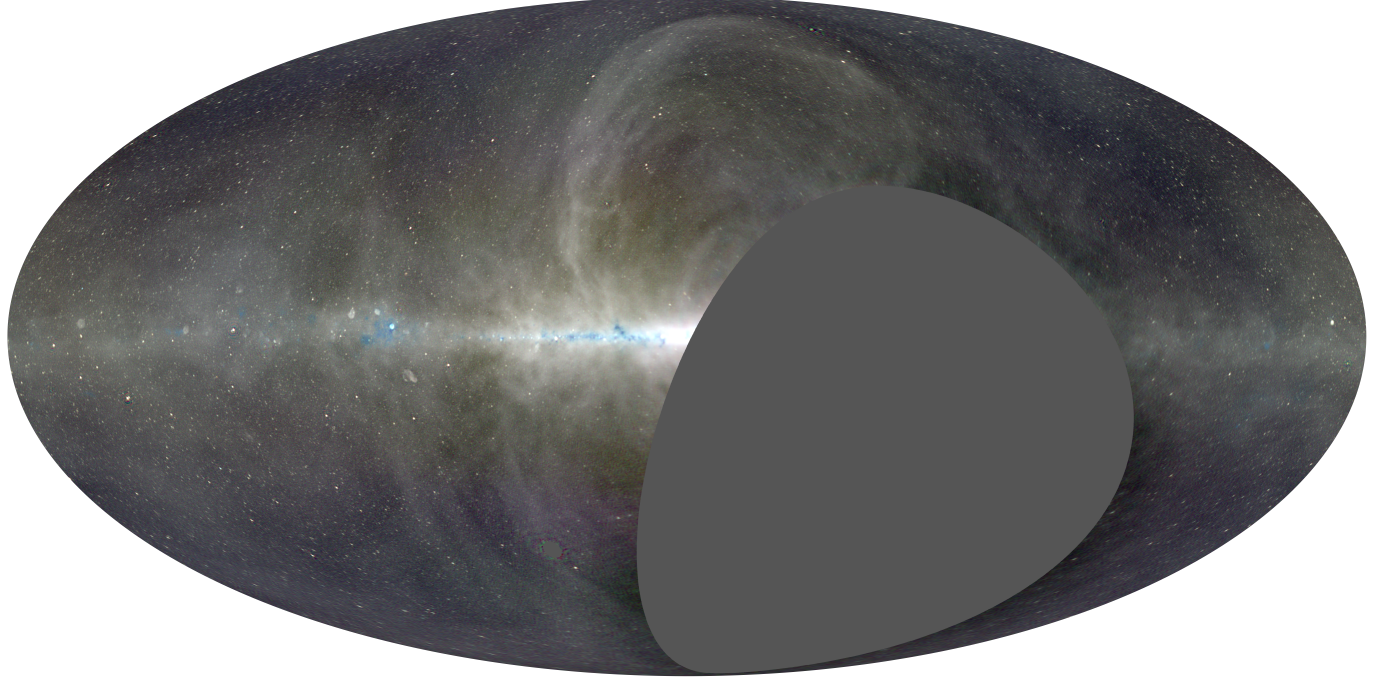
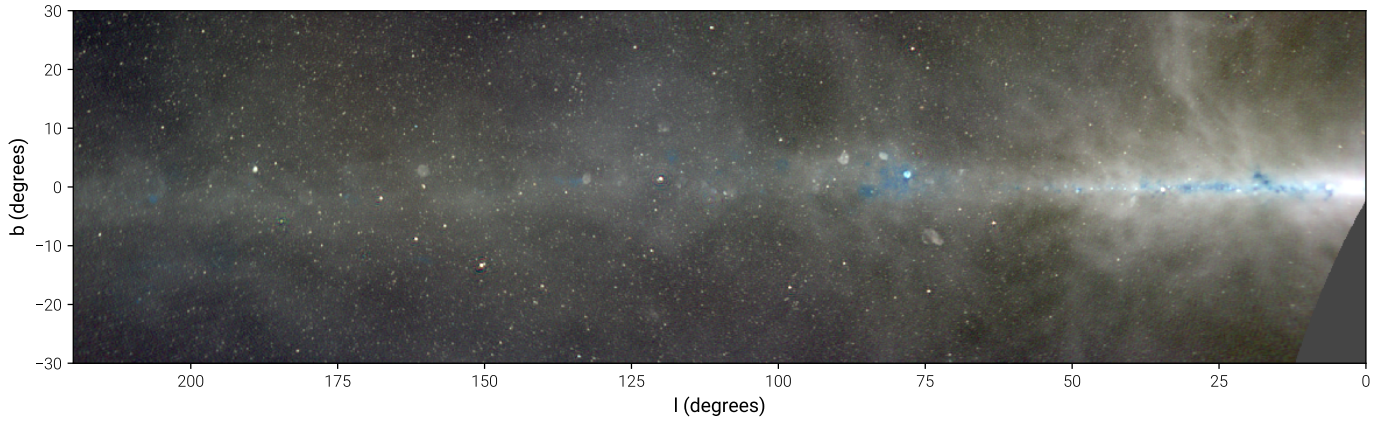


Figure 8. continued



**Figure 9.** This Mollweide-projected map is constructed from three maps of the sky at 36.528 MHz (red), 52.224 MHz (green), and 73.152 MHz (blue). The maps are scaled by  $\nu^{2.5}$  before combining and the color scale is logarithmic (as in Figure 8). Therefore, regions with a spectral index of  $-2.5$  will tend to appear white, and regions with a flatter spectral index will tend to appear blue.



**Figure 10.** A cutout of the galactic plane from Figure 9.

ear correlation between 36.528 MHz and 73.152 MHz. However, if  $R^2 \ll 1$ , the spectral index calculation is unreliable.  $R^2$  tends to drop in cold patches of the sky where there is not enough dynamic range to find a strong correlation between the two frequencies.  $R^2$  also tends to drop in the vicinity of H II regions in the galactic plane due to multiple emission mechanisms violating the assumption of a single spectral index. Therefore, we should restrict our interpretation of Figure 11 to the galactic plane and north galactic spur. In the galactic plane, the synchrotron spectral index varies between  $\sim -2.5$  and  $-2.75$ . In the vicinity of H II, regions the

spectral index flattens significantly. These H II regions can be seen with higher resolution in Figure 10. In Figure 10, H II regions appear as blue shadows along the galactic plane due to the increasing impact of free-free absorption at lower frequencies.

In the literature, the spectral index at low frequencies is commonly computed with respect to the Haslam 408 MHz map (Haslam et al. 1981, 1982), which was reprocessed by Remazeilles et al. (2015) to remove artifacts associated with  $1/f$  noise and bright sources. Figure 12 displays the spectral index computed between the 73.152 MHz map and the reprocessed Haslam

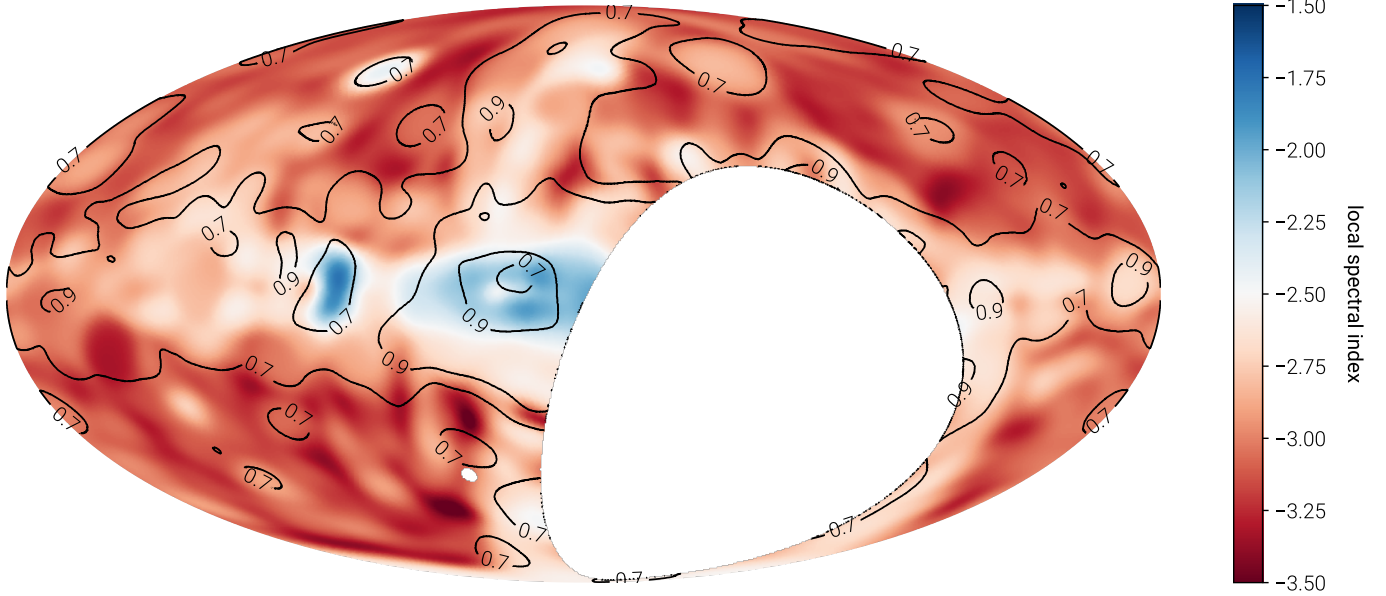


**Figure 11.** The local spectral index measured between the 36.528 MHz map and the 73.152 MHz map estimated by means of a local T-T plot. The color scale gives the spectral index where blue is flat spectrum and red is steep spectrum. The contours give the coefficient-of-determination ( $R^2$ ) for the linear fit to the local T-T plot. If  $R^2$  is low, the quality of the fit is low and the estimated spectral index is unreliable. This can be either due to insufficient dynamic range in the local T-T plot or due to multiple emission mechanisms operating in close proximity. Consequently  $R^2$  tends to drop at higher galactic latitudes (due to dynamic range), and near H II regions in the galactic plane (due to multiple emission mechanisms).

#	$\nu$ MHz	$\Delta\nu^a$ MHz	FWHM <sup>b</sup>			Noise <sup>c</sup> K	Noise <sup>c</sup> mJy/beam	Fraction of Modes <sup>d</sup> with $\sigma > \sqrt{\varepsilon}$
			$\delta = 0^\circ$	$\delta = +45^\circ$	$\delta = +75^\circ$			
1	36.528	0.024	$26.0' \times 19.1'$	$20.2' \times 16.9'$	$19.8' \times 18.7'$	595.	799.	0.391
2	41.760	0.024	$23.3' \times 17.5'$	$18.5' \times 16.0'$	$18.3' \times 17.4'$	541.	824.	0.480
3	46.992	0.024	$20.9' \times 16.3'$	$17.4' \times 15.2'$	$17.6' \times 16.9'$	417.	717.	0.504
4	52.224	0.024	$18.7' \times 15.2'$	$16.2' \times 15.0'$	$16.0' \times 15.8'$	418.	814.	0.535
5	57.456	0.024	$18.0' \times 14.9'$	$15.9' \times 15.0'$	$15.7' \times 15.4'$	354.	819.	0.542
6	62.688	0.024	$17.8' \times 15.0'$	$15.8' \times 14.9'$	$15.7' \times 15.4'$	309.	843.	0.540
7	67.920	0.024	$17.6' \times 15.0'$	$15.9' \times 14.7'$	$15.8' \times 15.6'$	281.	894.	0.529
8	73.152	0.024	$18.6' \times 15.1'$	$16.8' \times 14.6'$	$16.6' \times 16.1'$	154.	598.	0.512

<sup>a</sup> Bandwidth used to construct the map. As described in the text, each map is constructed from a single frequency channel (24 kHz).

<sup>b</sup> The full-width half-maximum (FWHM) of the synthesized beam at the specified declination (major axis  $\times$  minor axis).

<sup>c</sup> Measured with a jackknife and splitting the dataset into even- and odd-numbered integrations. This estimate therefore includes all noise sources that act on the timescale of a single 13 second integration (eg. thermal, ionospheric, etc.).

<sup>d</sup> Singular values of the transfer matrix compared with the value of the regularization parameter  $\varepsilon$  used while solving Equation 9. As discussed in the text, singular vectors with corresponding singular values  $\sigma \ll \sqrt{\varepsilon}$  are set to zero by the Tikhonov regularization procedure.

**Table 1.** A summary of the generated all-sky maps.

map. The spectral index was estimated by degrading the 73.152 MHz map to the resolution of the Haslam map and constructing local T-T plots in every direction. The coefficient-of-determination is overlaid as a contour plot, however because  $\log(408 \text{ MHz}/73.152 \text{ MHz}) > \log(73.152 \text{ MHz}/36.528 \text{ MHz})$ , the spectral indices presented in Figure 12 tend to be more robust than those

presented in Figure 11. This is reflected by the fact that  $R^2$  is larger, but the interpretation must still generally be restricted to the galactic plane.

#### 4.1. Comparisons with Other Sky Maps

##### 4.1.1. LWA1 Low Frequency Sky Survey

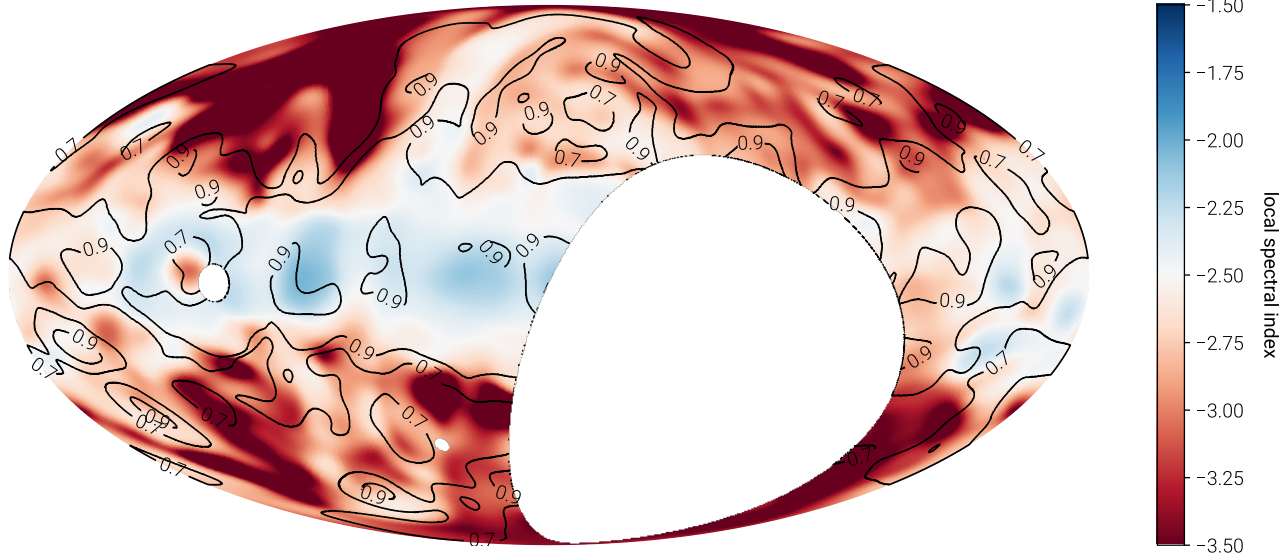


**Figure 12.** The local spectral index measured between the 73.152 MHz OVRO-LWA map and the reprocessed 408 MHz Haslam map (Remazeilles et al. 2015). The color scale gives the spectral index where blue is flat spectrum and red is steep spectrum. The contours give the coefficient-of-determination ( $R^2$ ) for the linear fit to the local T-T plot. See the caption of Figure 11 for more details about the coefficient-of-determination..

The LWA1 Low Frequency Sky Survey (LLFSS) (Dowell et al. 2017) produced nine maps of the sky between 35 MHz and 80 MHz. Six of these maps are interior to the frequency range spanned by this work. **Initial comparisons with the LLFSS helped characterize a systematic rotation in the LWA1’s antenna positions. After phase-calibration, this manifested itself as a systematic rotation and translation in the snapshot images that were mosaicked to form the final sky map. This systematic error has been corrected in the comparisons presented here and in the latest version of the LLFSS<sup>7</sup>.**

A direct comparison with these updated LLFSS maps can be seen in Figure 13. In this figure, the LLFSS maps are filtered to remove the monopole and all modes with  $m = 0$ . The OVRO-LWA maps are interpolated in frequency and blurred to match the angular resolution of the corresponding LLFSS map. At 60 MHz, the agreement is generally better than 10%. However at lower frequencies the agreement deteriorates to about 20%. Typically the OVRO-LWA maps have excess emission in the galactic plane and a deficit of emission off the galactic plane relative to the LLFSS.

The LLFSS incorporates calibrated total power radiometry to estimate the missing flux from short spac-

ings. As a result Dowell et al. (2017), report per-pixel spectral-indices from combining all nine sky maps. Care must be taken in comparing these spectral indices with Figure 11 because they are susceptible to different systematic errors. Both calculations are sensitive to mistakes in the antenna primary beam, but the LLFSS spectral indices are additionally sensitive to errors in the zero-level. We will restrict the comparison to the galactic plane where the spectral indices are likely to be the most reliable. Towards the galactic center both surveys agree that the spectral index is very flat ( $> -2.2$ ) due to the influence of free-free absorption. However, at galactic latitudes  $\sim 180^\circ$  this work suggests that the spectral index varies between -2.5 and -2.75, while the LLFSS reports substantially flatter indices in the range -2.3 to -2.2. In this region  $0.7 < R^2 < 0.9$  for the OVRO-LWA, so this could be an artifact of the comparatively weak correlation between the brightness at 36.528 MHz and 73.152 MHz, which tends to bias the spectral index towards  $-\infty$ .

The LLFSS also computes spectral indices with respect to the Haslam 408 MHz map. These spectral indices are subject to the same caveats and systematic errors as before. However, in general the qualitative agreement with Figure 12 is better, potentially due to the increased robustness associated with estimating spectral indices with a larger fractional bandwidth.

#### 4.1.2. Guzmán 45 MHz Map

The Guzmán 45 MHz map (Guzmán et al. 2011) is compiled from a southern hemisphere survey (Alvarez

<sup>7</sup> Available for download at: <http://lwa10g.alliance.unm.edu/LWA1LowFrequencySkySurvey/>

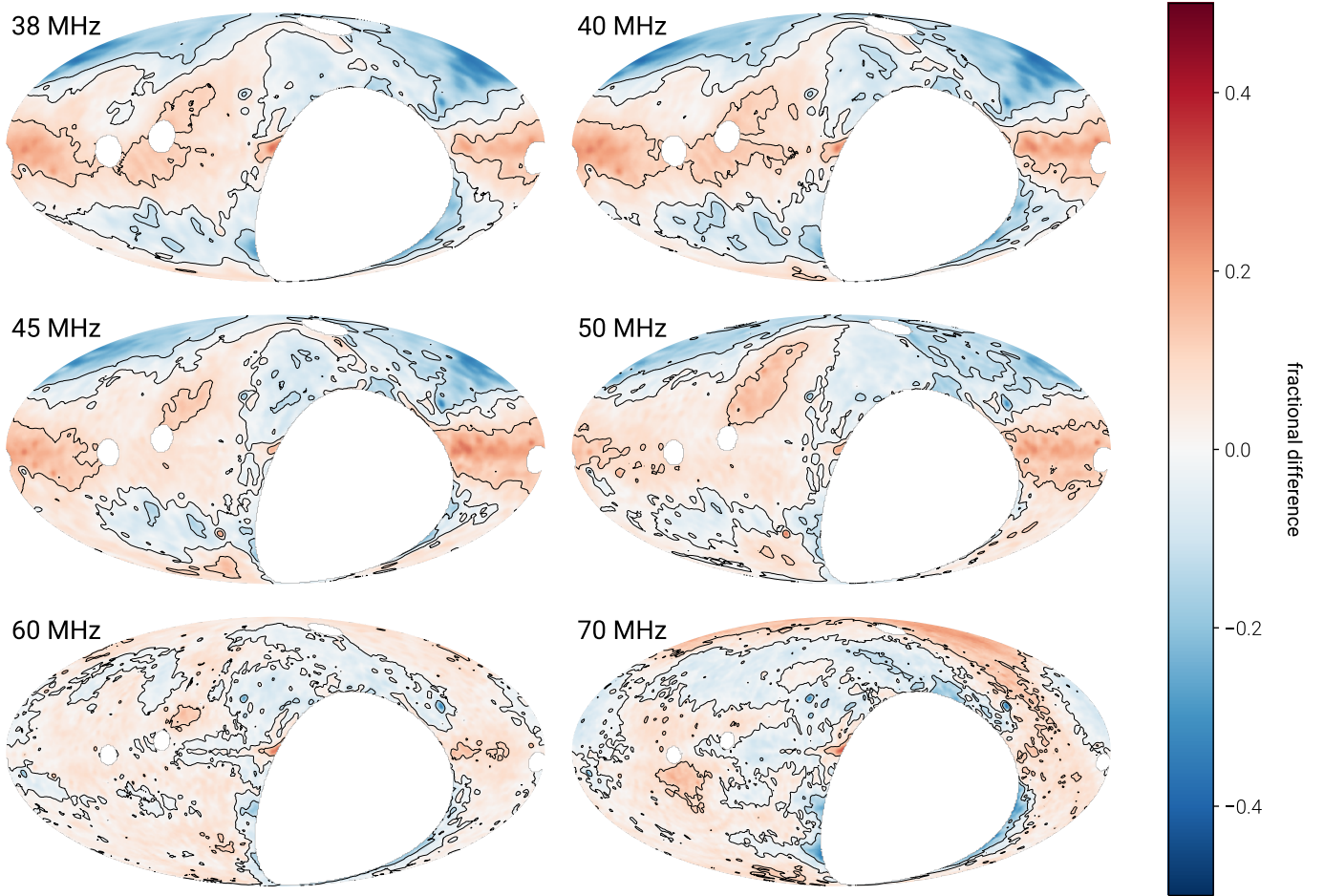


**Figure 13.** The fractional difference between maps from the LWA1 Low Frequency Sky Survey and the OVRO-LWA maps (Figure 8) after interpolating to the corresponding frequency and smoothing to the corresponding resolution. A positive value indicates regions where the OVRO-LWA map has more emission than the corresponding LWA1 Low Frequency Sky Survey map. Cas A, Cyg A, Vir A, and Tau A are masked due to the fact that they are subtracted from the OVRO-LWA maps.

et al. 1997) and a northern hemisphere survey (Maeda et al. 1999) with a small gap around the NCP. In this work, the zero-level is set by comparing against published low-frequency measurements in six different directions.

A direct comparison between the OVRO-LWA maps interpolated to 45 MHz and the Guzmán 45 MHz map can be seen in Figure 14. In order to make this comparison, the OVRO-LWA map was degraded to a  $5^\circ$  resolution by convolving with a Gaussian kernel, and the Guzmán map has had spherical harmonics with  $m = 0$  discarded in order to make it consistent with the maps presented in this paper. This figure shows a  $\sim 20\%$  excess of emission in the galactic plane that is consistent with the discrepancy observed between the LLFSS and the Guzmán map. However, while the LLFSS has an excess of emission near the north galactic pole, no such excess is observed in this work. Instead there is a 10% excess of emission near the south galactic pole. Else-

where off the plane of the galaxy the discrepancy can be as much as  $-20\%$ .

Guzmán et al. (2011) compute the spectral index between their 45 MHz map and the 408 MHz Haslam map. Along the galactic plane the spectral index varies between -2.2 (in the vicinity of H II regions), and -2.5 (at galactic longitudes  $\sim 180^\circ$ ). The north galactic spur has a spectral index of -2.5. This is generally consistent with the results presented in Figure 12.

## 5. ERROR ANALYSIS

### 5.1. The Ionosphere

One of the key assumptions made by  $m$ -mode analysis is that the sky is static. We assume that the only time-dependent behavior is the rotation of the Earth, which slowly rotates the sky through the fringe pattern of the interferometer. At low frequencies, the ionosphere violates this assumption. In particular, ionospheric scintil-

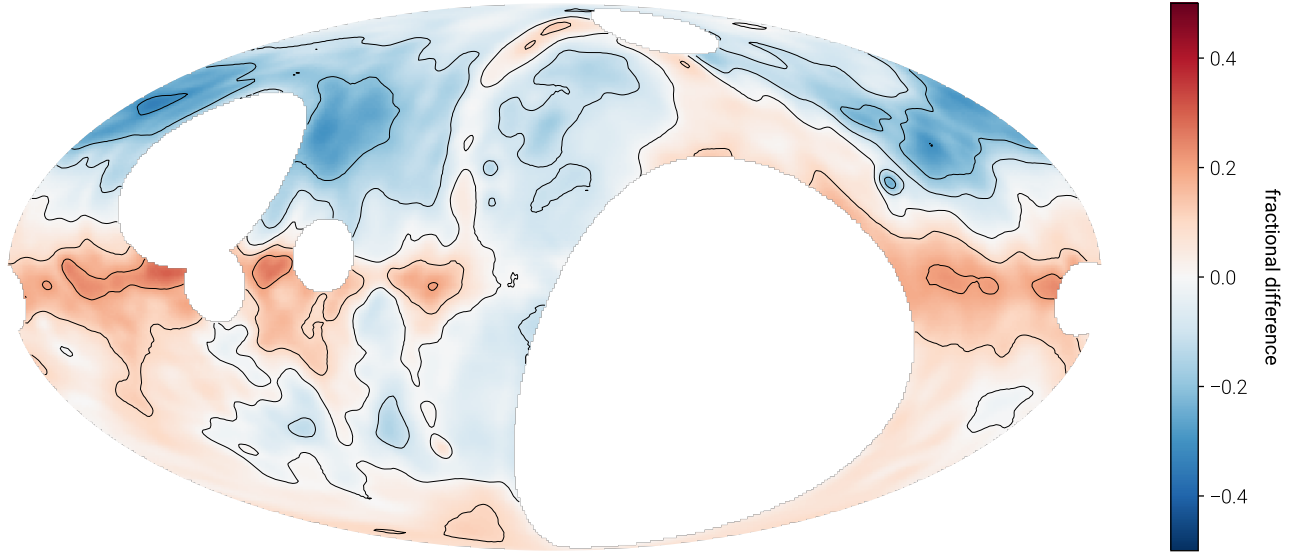


**Figure 14.** This Mollweide projected map compares the fractional difference between the Guzmán 45 MHz map, and the OVRO-LWA maps (Figure 8) interpolated to 45 MHz (degraded to  $5^\circ$  resolution). A positive value indicates regions where the OVRO-LWA map has more emission than the Guzmán map, and a negative value indicates regions where the Guzmán map has more emission than the OVRO-LWA map. Cas A, Cyg A, Vir A, and Tau A are masked due to the fact that they are subtracted from the OVRO-LWA maps but not the Guzmán map.

lation and refractive offsets will cause even static sources to exhibit significant variability (Figure 5).

The correlation observed on a given baseline for a single point source is

$$V_\nu(t_{\text{sidereal}}) = I_\nu B_\nu(t_{\text{sidereal}}), \quad (19)$$

where  $I_\nu$  is the flux of the source at the frequency  $\nu$ , and  $B_\nu$  is the baseline transfer function defined by Equation 3. The transfer function is a function of the direction to the source, which is in turn a function of the sidereal time  $t_{\text{sidereal}}$ . If the source is varying, from intrinsic variability or due to scintillation, than the source flux is also a function of the time coordinate  $t$  such that

$$V_\nu(t_{\text{sidereal}}) = I_\nu(t) B_\nu(t_{\text{sidereal}}), \quad (20)$$

where  $t_{\text{sidereal}} = (t \bmod 23^h 56^m)$ .

In order to compute the  $m$ -modes we must take the Fourier transform with respect to the sidereal time. As a consequence of the Fourier convolution theorem we find:

$$V_{\nu,m} \sim \sum_{m'} V_{\nu,m'}^{\text{static}} I_{\nu,m-m'}, \quad (21)$$

where  $V_{\nu,m}^{\text{static}}$  is the set of observed  $m$ -modes if the source was actually static, and  $I_{\nu,m-m'}$  is the Fourier transform of the light curve  $I_\nu(t)$ . Equation 21 indicates that power is scattered between different values of  $m$ . As a consequence, the true transfer matrix, which is exactly block diagonal in the ideal case, is no longer truly block diagonal (Shaw 2016).

The maps presented in Figure 8 do not account for any off-diagonal terms arising from ionospheric fluctuations. The effect of this can be seen in Figure 15. In this simulation, a point source is placed at the location of Cas A. In one case the source is allowed to scintillate in the same way Cas A does in Figure 5, but the source is always located exactly at the location of Cas A. In the second case the source position is allowed to vary in the same way Cas A does in Figure 5, but the flux of the source exactly traces the beam model. The scintillation, although large, introduces only  $< 0.3\%$  errors in the vicinity of bright point sources. Refractive offsets, however, can introduce  $\sim 15\%$  errors at 36.528 MHz and  $\sim 5\%$  errors at 73.152 MHz. Because the sidelobes of the PSF are altered from that of the ideal PSF, refractive offsets will restrict the dynamic range it is possible to obtain with the CLEAN algorithm described in §2.3. This effect can be clearly seen in Figure 16, where 10% errors within  $1^\circ$  of 3C 134 are seen at 36.528 MHz. As expected for an ionospheric effect these errors decrease to a few percent at 52.224 MHz, and less at 73.152 MHz. We therefore conclude that ionospheric effects directly limit the dynamic range in the vicinity of bright point sources.

## 5.2. Beam Errors

A model of the antenna beam is essential for widefield imaging. Because  $m$ -mode analysis imaging operates on a full sidereal day of data, images are constructed after watching each point in the sky move through a large

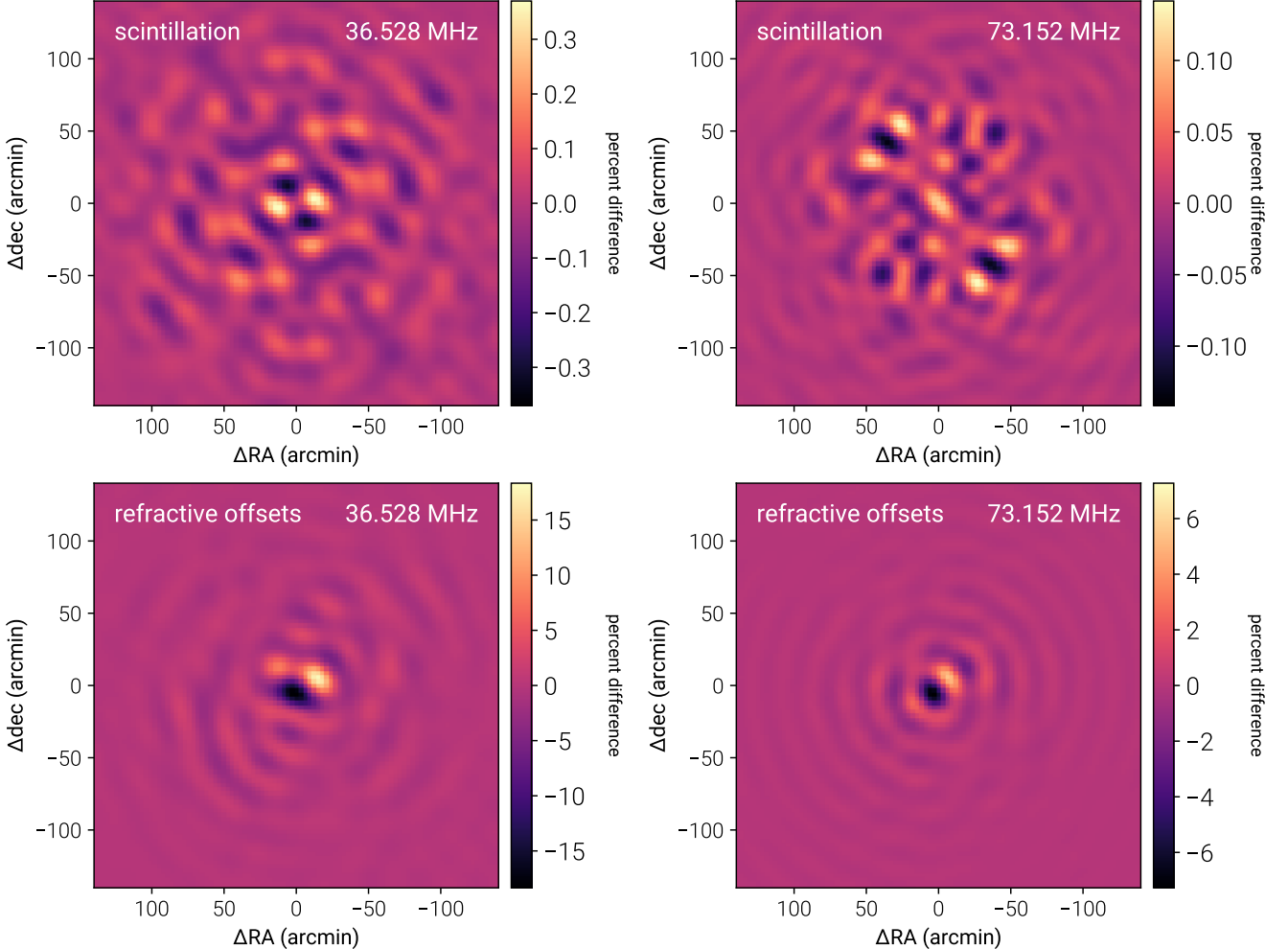


**Figure 15.** Illustration of the corrupting influence of the ionosphere at 36.528 MHz (left column) compared with 73.152 MHz (right column). Each panel shows the *simulated* PSF for a source at the location of Cas A, and illustrates the percent difference (relative to the peak flux of the uncorrected PSF) due to including an ionospheric effect. In the top row, the simulated source scintillates using the measured light-curve for Cas A in Figure 5. In the bottom row, the simulated source is refracted from its true position using the measured refractive offsets for Cas A in Figure 5.

slice of the beam (excepting the celestial poles). The beam model therefore serves two purposes:

1. setting the flux scale as a function of declination
2. reconciling observations from two separate sidereal times

In the first case, all sources at a given declination take the same path through the antenna primary beam. If the antenna response is overestimated along this track, then all sources at this declination will have underestimated fluxes. Similarly, if the antenna response is underestimated, then all the sources will have overestimated fluxes. The errors in Figure 7 do not show a clear pattern with declination. Two sources have a clear systematic offset at all frequencies: 3C 353 and 3C 380. 3C 353 is the second southernmost source, but Hya A

– the first southernmost source – does not exhibit this systematic error. Similarly, 3C 380 is at a comparable declination to Lyn A, which appears, if anything, to have its flux systematically offset in the other direction. The absence of a coherent pattern does not eliminate the possibility of beam errors effecting the flux scale, but it does mean that these errors are at least comparable to the errors inherent to the flux scale itself.

The second case is more subtle. Sources are observed at a wide range of locations in the primary beam of the antenna. The imaging process must reconcile all of these observations together, and the beam model provides the instructions for how to do this. In the event of an error in the beam model, it can be expected that the beam will introduce errors into the sky maps that will limit the dynamic range in the vicinity of bright point sources. Shaw et al. (2015) simulate the effect of beam errors on

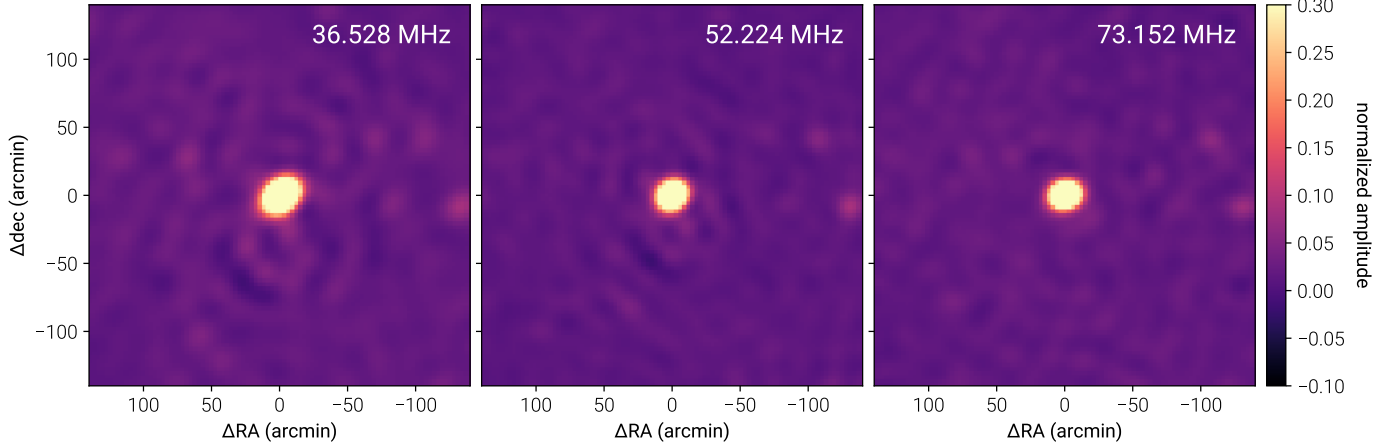


**Figure 16.** A zoom-in of 3C 134 at 36.528 MHz (left panel), 52.224 MHz (middle panel), and 73.152 MHz (right panel). At 36.528 MHz there are  $\sim 10\%$  artifacts around 3C 134 that persist after CLEANing due to ionospheric effects. As expected for an ionospheric origin, these artifacts decrease in amplitude as frequency increases. Figure 15 shows the typically expected amplitude of these effects for ionospheric scintillation and refractive offsets.

a cosmological analysis concluding that the beam must be known to one part in  $10^4$ . Our requirements are significantly less stringent because we are estimating the sky brightness instead of estimating the amplitude of a faint cosmological signal in the presence of foreground emission that dominates the signal by five orders of magnitude. In fact, in §5.1 we found that ionospheric effects likely dominate over other sources of error that affect the PSF shape. Therefore we conclude that the beam models generated in §3.3 are sufficient to limit the effect of beam errors on the PSF to at least less than those introduced by the ionosphere.

### 5.3. Polarization Leakage

Shaw et al. (2015) describe how to generalize  $m$ -mode analysis to account for a polarized sky observed with a polarized antenna beam. Heretofore this generalization has been neglected in the discussion of  $m$ -mode analysis imaging. At low frequencies, increasingly rapid Faraday rotation leads to depolarization. Therefore polarization fractions are generally expected to decrease at low frequencies (varying with ionospheric conditions). Lenc et al. (2016) detected the presence of diffuse polarized emission on degree angular scales with the MWA, also finding typical depolarization ratios of  $\sim 0.3$  for pulsars at 154 MHz relative to 1.4 GHz, although there was a large variance between pulsars. Even more depolarization is expected at frequencies  $\leq 73.152$  MHz, but crossed-dipole antennas with extremely large primary beams will naturally introduce large polarization leakage terms at low elevations. It is instructive to compute what impact this will have on the unpolarized imaging process.

In order to understand the effect of polarization leakage, we simulated a point source with 10% polarization

in Stokes- $Q$  at the location of Cas A. The simulated visibilities were computed using the measured beams for  $x$ - and  $y$ -dipoles. Because the amplitude of the two beams are not equal in every direction on the sky, this introduces a direction-dependent leakage of Stokes- $Q$  into Stokes- $I$ . At 73.152 MHz, this leakage is  $\lesssim 5\%$  above  $15^\circ$  elevation, but rapidly rises to  $\gtrsim 50\%$  at lower elevations. Obenberger et al. (2015) report similar polarization leakage measurements with the LWA1. Cas A is a circumpolar source and spends about seven hours every day skirting the horizon where the polarization leakage is large, so by placing the simulated source at the location of Cas A, we are engineering a situation where the polarization leakage from Stokes- $Q$  into Stokes- $I$  will be large. However, the impact on the unpolarized  $m$ -mode analysis maps is mild, amounting to a 0.5% error in the flux of the source.

### 5.4. Terrestrial Interference and Pickup

When writing Equation 2, it is implicitly assumed that the correlated voltage fluctuations measured between pairs of antennas are exclusively generated by astronomical sources of radio emission. In practice, this assumption can be violated. For instance, a low-frequency interferometer located in the vicinity of an arcing power line will see an additional contribution from the radio-frequency interference (RFI) generated by the arcing process. Similarly, common-mode pickup along the analog signal path of the interferometer may generate an additional spurious contribution to the measured visibilities. While the amplitude and phase of these contaminating signals may fluctuate with time, they do not sweep across the sky at the sidereal rate characteristic of astronomical sources.

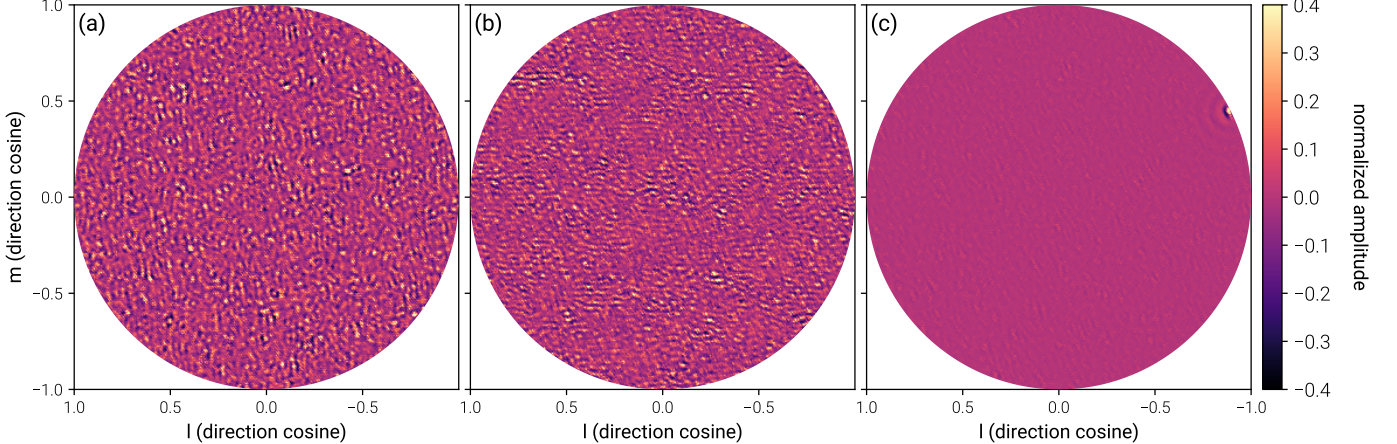


**Figure 17.** Terrestrial sources of correlated noise that are apparent after averaging the visibilities at 62.688 MHz over the entire 28 hour observing period (keeping the phase center at zenith such that astronomical sources of radio emission are smeared along tracks of constant declination). Each panel represents a different component that is removed from the visibilities. The images are generated using WSClean (Offringa et al. 2014), uniform weighting, and only baselines longer than 15 wavelengths. Panels (a) and (b) illustrate components that appear noise-like in image-space, but are in fact a constant-offset to the measured visibilities likely associated with cross-talk or common-mode pickup. Panel (c) illustrates a component that is clearly associated with an RFI source on the horizon to the west-north-west of the OVRO-LWA. This RFI source is likely an arcing power line. Figure 18 illustrates the characteristic ring-like artifacts introduced into the maps if these 3 components are not removed prior to  $m$ -mode analysis imaging. The component shown in panel (a) has about twice the amplitude ( $\|\mathbf{B}^* \mathbf{v}_{\text{terrestrial}}\|$ ) of panels (b) and (c), and for all three components  $\|\mathbf{B}^* \mathbf{v}_{\text{terrestrial}}\| / (\|\mathbf{B}\| \|\mathbf{v}_{\text{terrestrial}}\|) \sim 0.035$ .

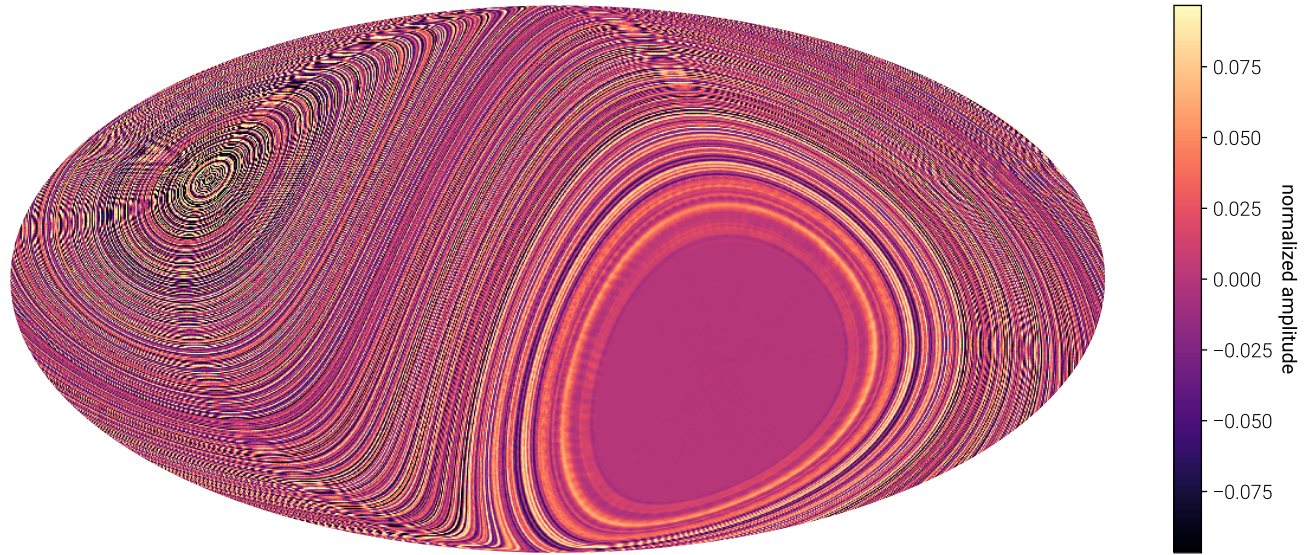


**Figure 18.** A Mollweide-projected image of the artifacts introduced to the  $m$ -mode analysis maps by the three terrestrial sources shown in Figure 17. Because these sources are not moving through the sky sidereally, they tend to be smeared along rings of constant declination. The spurs seemingly radiating from the north celestial pole are a Moiré pattern (ie. an artifact of the pixelization).

The Owens Valley is an important source of water and power for the city of Los Angeles. Unfortunately, this means that high voltage power lines run along the valley  $\gtrsim 10$  km to the west of the OVRO-LWA. Some of these power line poles have faulty insulators that arc and produce pulsed, broadband RFI. Because these poles exist in the near-field of the array, we have been able to local-

ize some of them by using the curvature of the incoming wavefront to infer a distance. Efforts are currently underway to work with the utility pole owners to have these insulators replaced.

In the meantime, it is possible to suppress their contamination in the dataset. The contribution of these RFI sources to the visibilities can be plainly seen by

averaging  $> 24$  hours of data with the phase center set to zenith. In this way, true sky components are smeared along tracks of constant declination while terrestrial sources (ie. the arcing power lines or any contribution due to common-mode pickup) are not smeared. Obtaining a model for the RFI is complicated by the fact that the contaminating sources are at extremely low elevations where the antenna response is essentially unknown (and inhomogeneous due to antenna shadowing effects). It is not enough to know the physical location of the faulty insulator generating the RFI. In addition, we must know the response of each antenna (amplitude and phase) in the appropriate direction. This motivates the use of peeling, which allows the antenna response to be a free parameter. Therefore, model visibilities for the RFI can be obtained by peeling the sources after smearing the visibilities over  $> 24$  hours. Figure 17 shows an illustration of some of the removed components at 62.688 MHz.

While attempting to peel RFI sources from the averaged visibilities, it was discovered that frequently peeling would remove components from the visibilities that are not obviously associated with any source on the horizon or elsewhere in the sky (see panels (a) and (b) in Figure 17). These components appear noise-like in the images, but they are actually a constant offset to the measured visibilities and are therefore likely associated with cross-talk or some form of common-mode pickup. If these components are not subtracted from the measured visibilities, they contribute ring-like structures into the sky maps as seen in Figure 18. This figure is not a simulation, but rather a difference between maps created before and after measuring and subtracting the components in Figure 17 from each integration.

The first step in Equation 9 is to compute  $\mathbf{B}^* \mathbf{v}$ . In this step we compute the projection of the measurement  $\mathbf{v}$  onto the space spanned by the columns of  $\mathbf{B}$ . Each column of  $\mathbf{B}$  describes the interferometer's response to a corresponding spherical harmonic coefficient of the sky brightness distribution. Therefore, the act of computing  $\mathbf{B}^* \mathbf{v}$  is to project the measured  $m$ -modes onto the space of  $m$ -modes which could be generated by astronomical sources. The degree to which a source of terrestrial interference will contaminate a map generated using  $m$ -mode analysis imaging is determined by its amplitude after projection.

For instance, a bright interfering source might contribute  $\mathbf{v}_{\text{terrestrial}}$  to the measured  $m$ -modes. However, if  $\mathbf{v}_{\text{terrestrial}}$  is actually perpendicular to all of the columns of  $\mathbf{B}$ , there will be no contamination in the map because  $\mathbf{B}^* \mathbf{v}_{\text{terrestrial}} = \mathbf{0}$ . In practice this is unlikely. In general, the contamination is proportional to the overall

amplitude of the interference ( $\|\mathbf{v}_{\text{terrestrial}}\|$ ) and the degree to which the interference mimics an astronomical signal ( $\|\mathbf{B}^* \mathbf{v}_{\text{terrestrial}}\| / (\|\mathbf{B}\| \|\mathbf{v}_{\text{terrestrial}}\|)$ ).

These terrestrial sources do not rotate with the sky and hence their contamination tends to be restricted to modes with small  $m$ . In this dataset the contamination is largely restricted to  $m \lesssim 1$ . Although the RFI is capable of fluctuating on short timescales, in this case the artifacts it introduces seem to be restricted to small  $m$  (presumably because the phase is not fluctuating). As a result if the contamination is not suppressed, it will manifest itself as rings along stripes of constant declination. This effect is plainly visible in Figure 17. Because of the distinctive ring-like pattern created by terrestrial sources, we additionally chose to discard spherical harmonics with either  $m = 0$  or  $m = 1$  and  $l > 100$  in order to further suppress the contamination.

## 6. CONCLUSION

In this work we presented a new imaging technique – Tikhonov regularized  $m$ -mode analysis imaging and CLEANing – for drift-scanning telescopes like the OVRO-LWA. This technique exactly corrects for wide-field effects in interferometric imaging with a single synthesis imaging step. We applied Tikhonov regularized  $m$ -mode analysis imaging to a 28 hour dataset and generated eight sky maps between 36.528 MHz and 73.152 MHz. These sky maps are a substantial improvement in angular resolution over existing maps at these frequencies with  $\sim 15$  arcmin angular resolution and  $< 600$  K thermal noise. The point source flux scale is consistent with that defined by Scaife & Heald (2012) to about 5% and large angular scales are consistent with the work of Dowell et al. (2017) to within 20%.

At frequencies above  $\sim 55$  MHz, the angular resolution of these maps is limited by the selection of  $l_{\max} = 1000$ . Future work will increase  $l_{\max}$  to remove this restriction, as well as include more time and bandwidth to improve the thermal noise. The usage of nighttime-only data can help mitigate dynamic range limitations from the ionosphere and also eliminate solar sidelobe residuals. Observations could also be extended to slightly higher and lower frequencies ( $\sim 27$  to 85 MHz) to take advantage of the full frequency range of the OVRO-LWA. The higher frequencies are particularly interesting in order to maximize the overlap with the MWA in the southern hemisphere, which could be used to fill-in the hole around the southern celestial pole.

These maps and future improvements are primarily intended to be used as part of a foreground modeling and subtraction routine for 21-cm cosmology experiments. Each map will be made publicly available on LAMBDA.

This work is dedicated to the memory of Professor Marjorie Corcoran, who was an influential mentor to MWE.

This material is based in part upon work supported by the National Science Foundation under Grant AST-1654815 and AST-1212226. The OVRO-LWA project was initiated through the kind donation of Deborah Castleman and Harold Rosen.

Part of this research was carried out at the Jet Propulsion Laboratory, California Institute of Technology, under a contract with the National Aeronautics and Space Administration, including partial funding through the President's and Director's Fund Program.

This work has benefited from open-source technology shared by the Collaboration for Astronomy Signal Pro-

cessing and Electronics Research (CASPER). We thank the Xilinx University Program for donations; NVIDIA for proprietary tools, discounts, and donations; Digicom for collaboration on manufacture and testing of DSP processors.

We thank the Smithsonian Astrophysical Observatory Submillimeter Receiver Lab for the collaboration of its members.

Development, adaptation, and operation of the LEDA real-time digital signal processing systems at OVRO-LWA has been supported in part by NSF grants AST/1106059, PHY/0835713, and OIA/1125087.

GBT, JD and FKS acknowledge support from the National Science Foundation under grant AST-1139974.

## REFERENCES

- Ali, Z. S., Parsons, A. R., Zheng, H., et al. 2015, *ApJ*, 809, 61
- Alvarez, H., Aparici, J., May, J., & Olmos, F. 1997, *A&AS*, 124, 205
- Baars, J. W. M., Genzel, R., Pauliny-Toth, I. I. K., & Witzel, A. 1977, *A&A*, 61, 99
- Beardsley, A. P., Hazelton, B. J., Sullivan, I. S., et al. 2016, *ApJ*, 833, 102
- Berger, P., Oppermann, N., Pen, U.-L., & Shaw, J. R. 2016, ArXiv e-prints, arXiv:1612.03255
- Bezanson, J., Edelman, A., Karpinski, S., & Shah, V. B. 2017, *SIAM Review*, 59, 65.  
<http://dx.doi.org/10.1137/141000671>
- Bhatnagar, S., Rau, U., & Golap, K. 2013, *ApJ*, 770, 91
- Bowman, J. D., Rogers, A. E. E., Monsalve, R. A., Mozdzen, T. J., & Mahesh, N. 2018, *Nature*, 555, 67
- Briggs, D. S. 1995, phdthesis, The New Mexico Institute of Mining and Technology
- Chapman, E., Abdalla, F. B., Bobin, J., et al. 2013, *MNRAS*, 429, 165
- Cornwell, T. J., Golap, K., & Bhatnagar, S. 2008, *IEEE Journal of Selected Topics in Signal Processing*, 2, 647
- de Oliveira-Costa, A., Tegmark, M., Gaensler, B. M., et al. 2008, *MNRAS*, 388, 247
- DeBoer, D. R., Parsons, A. R., Aguirre, J. E., et al. 2016, ArXiv e-prints, arXiv:1606.07473
- Dowell, J., Taylor, G. B., Schinzel, F. K., Kassim, N. E., & Stovall, K. 2017, *MNRAS*, 469, 4537
- Ewall-Wice, A., Dillon, J. S., Hewitt, J. N., et al. 2016, *MNRAS*, 460, 4320
- Fialkov, A., Barkana, R., Pinhas, A., & Visbal, E. 2014, *MNRAS*, 437, L36
- Furlanetto, S. R., Oh, S. P., & Briggs, F. H. 2006, *PhR*, 433, 181
- Greig, B., & Mesinger, A. 2015, *MNRAS*, 449, 4246
- Guzmán, A. E., May, J., Alvarez, H., & Maeda, K. 2011, *A&A*, 525, A138
- Górski, K. M., Hivon, E., Banday, A. J., et al. 2005, *ApJ*, 622, 759
- Hallinan, G., et al. in prep.
- Haslam, C. G. T., Klein, U., Salter, C. J., et al. 1981, *A&A*, 100, 209
- Haslam, C. G. T., Salter, C. J., Stoffel, H., & Wilson, W. E. 1982, *A&AS*, 47, 1
- Heald, G. H., Pizzo, R. F., Orrú, E., et al. 2015, *A&A*, 582, A123
- Helmboldt, J. F., & Kassim, N. E. 2009, *AJ*, 138, 838
- Högbom, J. A. 1974, *A&AS*, 15, 417
- Iijima, B. A., Harris, I. L., Ho, C. M., et al. 1999, *Journal of Atmospheric and Solar-Terrestrial Physics*, 61, 1205
- Intema, H. T., Jagannathan, P., Mooley, K. P., & Frail, D. A. 2017, *A&A*, 598, A78
- Johnson, S. G. 2008, The NLopt nonlinear-optimization package, <http://ab-initio.mit.edu/nlopt>, ,
- Kassim, N. E., Lazio, T. J. W., Erickson, W. C., et al. 2007, *ApJS*, 172, 686
- Kintner, Jr., P. M., Coster, A. J., Fuller-Rowell, T., et al. 2008, Washington DC American Geophysical Union Geophysical Monograph Series, 181, doi:10.1029/GM181
- Kocz, J., Greenhill, L. J., Barsdell, B. R., et al. 2015, *Journal of Astronomical Instrumentation*, 4, 1550003
- Lane, W. M., Cotton, W. D., van Velzen, S., et al. 2014, *MNRAS*, 440, 327
- Lenc, E., Gaensler, B. M., Sun, X. H., et al. 2016, *ApJ*, 830, 38

- Maeda, K., Alvarez, H., Aparici, J., May, J., & Reich, P. 1999, *A&AS*, 140, 145
- Mevius, M., van der Tol, S., Pandey, V. N., et al. 2016, *Radio Science*, 51, 927
- Mitchell, D. A., Greenhill, L. J., Wayth, R. B., et al. 2008, *IEEE Journal of Selected Topics in Signal Processing*, 2, 707
- Monsalve, R. A., Rogers, A. E. E., Bowman, J. D., & Mozdzen, T. J. 2017, *ApJ*, 847, 64
- Mozdzen, T. J., Bowman, J. D., Monsalve, R. A., & Rogers, A. E. E. 2017, *MNRAS*, 464, 4995
- Obenberger, K. S., Taylor, G. B., Hartman, J. M., et al. 2015, *Journal of Astronomical Instrumentation*, 4, 1550004
- Offringa, A. R., McKinley, B., Hurley-Walker, N., et al. 2014, *MNRAS*, 444, 606
- Parsons, A. R., Pober, J. C., Aguirre, J. E., et al. 2012, *ApJ*, 756, 165
- Patil, A. H., Yatawatta, S., Koopmans, L. V. E., et al. 2017, *ApJ*, 838, 65
- Perley, R. A., & Butler, B. J. 2017, *ApJS*, 230, 7
- Pober, J. C., Parsons, A. R., Jacobs, D. C., et al. 2012, *AJ*, 143, 53
- Price, D. C., Greenhill, L. J., Fialkov, A., et al. 2017, ArXiv e-prints, arXiv:1709.09313
- Pritchard, J. R., & Loeb, A. 2012, *Reports on Progress in Physics*, 75, 086901
- Refregier, A. 2003, *MNRAS*, 338, 35
- Remazeilles, M., Dickinson, C., Banday, A. J., Bigot-Sazy, M.-A., & Ghosh, T. 2015, *MNRAS*, 451, 4311
- Rowan, T. 1990, phdthesis, Department of Computer Sciences, University of Texas at Austin
- Salvini, S., & Wijnholds, S. J. 2014, *A&A*, 571, A97
- Scaife, A. M. M., & Heald, G. H. 2012, *MNRAS*, 423, L30
- Shaw, J. R. 2016, private communication, ,
- Shaw, J. R., Sigurdson, K., Pen, U.-L., Stebbins, A., & Sitwell, M. 2014, *ApJ*, 781, 57
- Shaw, J. R., Sigurdson, K., Sitwell, M., Stebbins, A., & Pen, U.-L. 2015, *PhRvD*, 91, 083514
- Singh, S., Subrahmanyam, R., Udaya Shankar, N., et al. 2017, ArXiv e-prints, arXiv:1703.06647
- Smirnov, O. M., & Tasse, C. 2015, *MNRAS*, 449, 2668
- Sokolowski, M., Tremblay, S. E., Wayth, R. B., et al. 2015, *PASA*, 32, e004
- Thompson, A. R., Moran, J. M., & Swenson, Jr., G. W. 2001, *Interferometry and Synthesis in Radio Astronomy*, 2nd Edition
- Turtle, A. J., Pugh, J. F., Kenderdine, S., & Pauliny-Toth, I. I. K. 1962, *MNRAS*, 124, 297
- Vedantham, H. K., & Koopmans, L. V. E. 2015, *MNRAS*, 453, 925
- Venumadhav, T., Chang, T.-C., Doré, O., & Hirata, C. M. 2016, *ApJ*, 826, 116
- Voytek, T. C., Natarajan, A., Jáuregui García, J. M., Peterson, J. B., & López-Cruz, O. 2014, *ApJL*, 782, L9
- Wayth, R. B., Lenc, E., Bell, M. E., et al. 2015, *PASA*, 32, e025
- Zheng, H., Tegmark, M., Dillon, J. S., et al. 2017a, *MNRAS*, 464, 3486
- . 2017b, *MNRAS*, 465, 2901